Radiation Pressure induced Nonlinearity in a Micro-droplet

Aram Lee

Dissertation submitted to the faculty of
the Virginia Polytechnic Institute and State University
in partial fulfillment of the requirements for the degree of

Doctor of Philosophy
in
Electrical Engineering

Yong Xu, Chair

Anbo Wang

Sunghwan Jung

Ting-Chung Poon

William T. Baumann

November 17, 2016
Blacksburg, Virginia

Keywords: Droplet resonator, Optofluidics, Single-photon nonlinearity
Radiation pressure, Fiber Bragg grating

Radiation Pressure induced Nonlinearity in a Micro-droplet

Aram Lee

ABSTRACT

Optical resonators such as silica micro-spheres and micro-toroids can support whispering gallery modes (WGMs), where light circulates near the resonator surface and is confined by the total internal reflection at the dielectric boundary. Such resonators can exhibit very high quality (*Q*) factors, since the resonator surface can maintain atomic level smoothness. The combination of high *Q* factors and small resonator volumes has led to a wide range of applications in sensing, optomechanics, nonlinear optics, and quantum optics.

In this dissertation, we introduce a new type of whispering gallery resonators (WGRs) based on micro-droplets in an immiscible liquid-liquid system. Within such an all-liquid platform, it is possible to achieve highly nonlinear coupling between light and liquid that can potentially lead to single-photon level optical nonlinearity. Specifically, we experimentally characterize a droplet ($D \simeq 500\,um$) of index matching fluid submerged in the water as a high-*Q* optical resonator, where we use an optical fiber taper to couple light into the droplet through non-contact evanescent coupling. The highest *Q*-factor observed in the experiment is 2×10^7 which closely matches the upper limit of intrinsic *Q*-factor set by the material absorption. Given with such a high *Q* factor, the WGM can exert strong radiation pressure on the droplet interface, push it outward, increase the length of optical path, and produce a red-shift in WGM resonance. Our experimental results have found that the ratio of those resonance shifts and the optical

power coupled into the resonator is approximately 60 fm/μW. The result closely matches to our steady-state estimation based on solving the coupled Maxwell-Navier-Stokes equation. To investigate the dynamic interplay of light and liquid, we develop a harmonic oscillator (HO) model to describe the time-domain behaviors of the coupled optofluidic system. We find a good agreement between theoretical predictions and our experimental data.

The shift of WGM resonance can potentially be induced by thermal effects. To estimate the magnitude of thermal effects, we also investigate the thermally induced nonlinear behaviors of WGMs in a cylindrical fiber resonator ($D \simeq 125\,um$), where we change the mechanism of heat dissipation by changing the cladding material (e.g. air and water). For direct temperature measurements, we use a fiber optical resonator with a fiber Bragg grating (FBG) inscribed in the fiber core to observe temperature shifts induced by the high-*Q* WGMs. Our result shows that the temperature increase in the fiber resonator in the water is 0.13 ^{o}C, whereas the fiber resonator in air shows ~4.5 ^{o}C increase in temperature. Our results suggest that the relatively high thermal conductivity of water suppresses thermal nonlinearity by ~50 times, and that the red-shifts of WGMs can largely be attributed to radiation pressure effect.

Radiation Pressure induced Nonlinearity in a Micro-droplet

Aram Lee

GENERAL AUDIENCE ABSTRACT

Optical resonators are used to confine incoming light and store its energy in a small volume. The quality of such resonators' optical confinement is represented by quality factor (*Q*). Among different types of optical resonators, whispering gallery resonator (WGR) is well known for its high-*Q*, where strong optical confinement is achieved by the total internal reflection at the curved internal surface of spherical / cylindrical dielectric volume. The combination of high *Q* factors and small resonator volumes has led to a wide range of applications in sensing, optomechanics, nonlinear optics, and quantum optics.

In this dissertation, we introduce a new type of WGR based on oil micro-droplet in water. Such an all-liquid platform enables highly nonlinear coupling between optical power and liquid matter that can potentially lead to optical nonlinearity at single-photon energy level. Specifically, we experimentally characterize an oil droplet ($D \simeq 500\,um$) submerged in the water as a high-*Q* optical resonator, where we use a tapered optical fiber to inject optical power into the droplet. The highest *Q* of whispering gallery mode (WGM) observed in our experiment is 2×10^7 and given with the high amplification of optical power in droplet, the WGM can exert strong radiation pressure on the droplet interface, push it outward, increase the length of optical path, and produce a red-shift in WGM resonance. Our experimental results have found that the ratio of those resonance

shifts and the optical power coupled into the resonator is approximately 60 fm/μW. The result closely matches to our steady-state estimation based on solving the coupled Maxwell-Navier-Stokes equation. To investigate the dynamic interplay of light and liquid, we develop a harmonic oscillator (HO) model to describe the time-domain behaviors of the coupled optofluidic system. We find a good agreement between theoretical predictions and our experimental data.

The shift of WGM resonance can potentially be induced by thermal effects. To estimate the magnitude of thermal effects, we also investigate the thermally induced nonlinear behaviors of WGMs in a cylindrical fiber resonator ($D \simeq 125\,um$), where we change the mechanism of heat dissipation by changing the media (e.g. air and water) surrounding the resonator. For direct temperature measurements, we use a fiber optical resonator with a temperature sensor equipped inside to observe temperature shifts induced by the high-*Q* WGMs. Our result shows that the temperature increase in the fiber resonator in the water is 0.13 ^{o}C, whereas the fiber resonator in air shows ~4.5 ^{o}C increase in temperature. Our results suggest that the relatively high thermal conductivity of water suppresses thermal nonlinearity by ~50 times, and that the red-shifts of WGMs can largely be attributed to radiation pressure effect.

Acknowledgement

The time I have spent at Virginia Tech was certainly fruitful and enjoyable. Virginia Tech not only opened the door to scientific research, but also broadened my view in many aspects to the world. I feel very grateful to spend part of my life in this wonderful place.

There are many people to thank for their support and encouragement. First and foremost, I am deeply indebted to my advisor Professor Yong Xu, for his tremendous help and guidance throughout my graduate study. It has been a great pleasure all the time to be his students. His fascination and deep understanding of optics with both fundamental and applied science are what have inspired me the most. While allowing and encouraging me to work independently, he was always ready to offer helpful suggestions and insightful comments. Without his guidance, I could not have appreciated the wondrous beauty of optics as much as I do now. I truly believe that his attitude toward the research will serve as a role model for me in the years to come.

I want to thank the members of my dissertation advisory committee: Profs. Anbo Wang, Sunghwan Jung, Ting-Chung Poon, and William T. Baumann for their useful comments and suggestions for the work included in this dissertation.

It has been such a valuable and pleasant experience to work in Center for Photonics Technology (CPT) that I will never forget. I would like to thank every colleagues for their helps and discussions: Dr. Jihaeng Yi, Dr. Islam Ashry, Dr. Ishac Kandas, Dr. Peng Lu, Dr. Chalongrat Daengngam, Dr. Dong Wang, Dr. Bo Liu, Dr. Michael Fraser, Dr. Cheng Ma, Jing Wang, Jeong-Ah Lee, Di Hu, Li Yu, Chengshuai Li, Ziang Feng, Tong Qui, Yun Dong, and Taylor Ray.

I would also like to thank Professor Thomas Mills, who generously gave me the access to his welding shop, where most of my nanoparticle sensing project has been done. Also Professor Yizheng Zhu gave me advices on optical interferometry systems and I was happy to learn how to efficiently organize experiments from an engineering perspectives. It was also a great pleasure to collaborate with Dr. Peng Zhang, who supported me with his broad knowledge in fluid mechanics for my optofluidics research.

Further gratitude is for my friends for their continual helps and unforgettable friendships: Woochan Kim, Hyunsoo Koh, Jaesung Jung, Kunjin Ryu, and Jaeeung Kim. Also I will never forget the lifelong cheers from all my friends back in my hometown: Inseop Choe, Jung Han Lee, and Du Hak Heo, who have always reminded me that I am not alone.

Finally, I would like to give my thanks to my parents. They have always been supporting me and offering me endless love and inspiration. Dear Mom and Dad, I am finally coming home.

Table of Contents

List of Figures

List of Table

List of Abbreviations

CTS	Component testing system
DAQ	Data acquisition
EM	Electromagnetic
EOM	Electro-optic modulator
FBG	Fiber Bragg grating
FP	Fabry-Perot
FSR	Free spectral range
HO	Harmonic oscillator
LS	Linear stage
MDR	Morphology dependent resonance
ODE	Ordinary differential equation
OSA	Optical spectrum analyzer
PC	Polarization controller
PD	Photo-detector
PZT	Piezo-electric transducer
Q	Quality factor
SM	Single mode
SMF	Single mode fiber
TE	Transverse electric
TM	Transverse magnetic
TIR	Total internal reflection
TL	Tunable laser
UV	Ultra-violet
WGM	Whispering gallery mode
WGR	Whispering gallery resonator

Chapter 1

Introduction

1.1 Motivation

The existence of whispering gallery mode (WGM) was first described by Lord Rayleigh in the 19th century after he found an interesting acoustic effect, where one person could hear a whisper from another person standing on the other side of a large church dome [1, 2]. He suggested that the curved surface of dome could guide the acoustic wave efficiently. The term ‘whispering gallery mode’ has since come to be applied to the electromagnetic (EM) wave travels primarily near the interface of a high index dielectric material, where optical confinement is produced by total internal reflection (TIR). As the optical resonances in these structures are a function of their morphology, they are sometimes referred to as morphology dependent resonances (MDRs) [3, 4]. The equations for resonant frequencies of dielectric and metallic spheres were first derived by Debye [5] in 1909, which could also be obtained by analyzing Mie scattering of plane waves by spheres in 1908 [6].

Optical resonators come in a variety of geometries and sizes, from the several kilometers of Fabry-Perot (FP) resonator at the Laser Interferometer Gravitational Wave Observatory (LIGO) [7-9] to the photonic crystal cavities at sub-wavelength scale [10-12]. Numerous researches on FP-type cavities have already been reported long before the emergence of practical researches on whispering gallery resonators (WGR). However, by overcoming the drawbacks of FP cavities (e.g. relatively low intrinsic *Q* factors and

requirements of sophisticated mirror fabrication and precise alignment), WGRs have attracted much attention, due to their numerous advantages such as ultra-high-*Q* factors, small mode volume, and compatibility with telecommunication technologies. In existing literatures, high-*Q* WGMs can be implemented in several distinct geometries that include spheres [13, 14], cylinders [15, 16], micro-rings [17, 18], micro-disks [19, 20], and micro-toroids [21, 22]. Those micron-scale WGRs are especially interesting for their potential applications including filtering [23, 24], lasing [25, 26], and sensing [16, 27-29].

Optomechanics have been an important area of research in past decades where it studies the dynamic interaction between light and solid structures [30–32]. To date, most researches regarding optomechanics uses solid resonators to investigate the nonlinear effects in micro-cavities [33–35]. Due to the high *Q*-factor of WGMs, the optical resonators can significantly reduce the optical power required to induce physical vibrations in the solid resonators. However, the rigid surface of such resonators seldom allows significant interfacial deformation.

Recently, optofluidics [36, 37] was introduced, with the aim of merging the areas of optics and microfluidics to achieve novel functionalities including integrated optics [38, 39], lasers [40], and sensing [41]. The relatively low interfacial tension of liquids can potentially allow significant deformation under low external force. Up to now, there have been a few of studies that investigate the mechanical interaction between optical field and fluids [42–47]. The earliest example is perhaps the classic work in [42], where a focused high power laser beam is used to create a bulge over a flat air-liquid interface. Similarly, in [44, 45], the authors used a high power laser beam focused onto a liquid droplet to distort its interface. More recently, optical radiation pressure was used in [46] to distort a

flat liquid interface and form a tunable lens. The existence of high-*Q* WGMs in a liquid droplet has also been experimentally confirmed [48, 49]. Also Dr. Tal Carmon group have recently reported the optical excitation of thermo-capillary vibration [50] and thermal nonlinearity [51] in the fluidic droplet resonator. The focus of our work, however, is distinct from the existing studies. Specifically, the ultimate goal of our research is to demonstrate that the radiation pressure of a high-*Q* WGM can lead to nonlinear optofluidic interactions that are very similar to classical third-order nonlinear processes such as Kerr effects. In particular, we note that the WGMs circulating around the equator of WGR can produce radiation pressure that can push the resonator interface outward and elongate the circumference of the droplet resonator. The geometrical deformation can in turn shift the resonances of WGMs. A major goal of this dissertation is to experimentally characterize the radiation pressure induced nonlinearity, and relate the resonance shifts of the WGM in a liquid droplet with the optical power coupled into the droplet resonator.

1.2 Thesis Organization

This research aims to investigate the nonlinearity induced by radiation pressure in fluidic droplet WGRs. More specifically, we aim to describe our study in the following orders:

- **Chapter 2:** This chapter introduces the most frequently used concepts in WGM research, where we discuss topics such as optical loss mechanisms and quality factors, finesse and free spectral range, notation of WGM mode numbers, and different techniques of WGM coupling.
- **Chapter 3:** We introduce the principles of three most important components in our study: WGM, radiation pressure, and fiber Bragg grating (FBG). The mode

characterization and field distribution (in radial, azimuthal, and polar dependences) of the spherical WGR is discussed. Also the fundamental principle of radiation pressure is presented. The mechanism of FBG based temperature sensing is also shortly introduced.

- **Chapter 4:** This chapter presents a theoretical analysis of the interaction between optically driven radiation pressure and the dynamic motion of fluidic interface. Starting from Young-Laplace equation, we estimate the scale of droplet deformation under steady-state. Then to predict the dynamic interaction of WGM resonance and deformed resonator shape in time domain, we build a harmonic oscillator (HO) model that couples the motion of droplet and the characteristic equation of WGM. Also simple linear steady-state estimation is derived where it directly relates the optical input power to the scale of resulting resonance shift.
- **Chapter 5:** We describe the experimental configuration for characterizing high-*Q* WGMs in a fluidic droplet resonator. Fabrication of single-mode tapered fiber is described. The parameters of the droplet resonator are also discussed. Several key aspects of experimental design, such as the requirement of high-*Q* factors and long evanescent tail for non-contact coupling, are analyzed. The experimental configuration used for WGM transmission measurement is shown.
- **Chapter 6:** We experimentally confirm the existence of high-*Q* WGM in droplet resonator. Then we vary the input power of the optical signals and measure the responses of the WGMs in the droplet resonator. We find that the WGM resonances in the droplet can experience significant red-shift under appropriate scanning conditions. Our experimental data is compared with HO model

predictions. We also describe the algorithm used to extract the value of resonance shift observed in the WGM transmission spectrum.

- **Chapter 7:** Comparative analysis of thermal nonlinearity in cylindrical WGRs in air as well as in water. Here, we use an optical fiber with a FBG written in the fiber core as the optical resonator, where optical absorption of the high-*Q* WGM confined near the fiber surface serves as a heat source. By measuring the spectral dependence of optical signals reflected by the FBG, we can measure temperature shift at the fiber core. Experimentally, we find that whether the WGR is immersed in air or in water can have significant impact on the temperature measured by the FBG. In this chapter, several unique characteristics of cylindrical WGMs are discussed.
- **Chapter 8:** We find that the predictions of the HO model closely match our experimental observations, which suggests that the experimentally observed red-shift in WGM resonances can indeed be attributed to radiation pressure. In this chapter, we theoretically investigate the feasibility of single-photon-level nonlinearity by estimating droplet deformation under extremely low optical input power. Based on the theoretical analysis, we identify the conditions that can lead to room temperature single-photon nonlinearity. At the end, we discuss a WGM coupling configuration modified from our current setup to demonstrate the μW–level optical switching.

References

1. L. Rayleigh, *Philos. Mag., vol*. 20, pp. 1001, 1910.

2. L. Rayleigh, *Scientific Papers*, vol. 5, pp. 617, 1912.

3. A. Ashkin and J. M. Dziedzic,"Observation of optical resonances of dielectric spheres by light scattering," *Appl. Opt*., Vol. 20, pp. 1803-1814 , 1981.

4. C. C. Lam, P. T. Leung, and K. Young, "Explicit asymptotic formulas for the positions, widths, and strengths of resonances in Mie scattering," *J. Opt. Soc. Am. B*, Vol. 9 pp. 1585, 1992.

5. P. Debye, "Der Lichtdruck auf Kugeln von beliebigem Material," *Ann. Phys.*, Vol. 30, pp. 57–136. 1909.

6. G. Mie, "Beitrage zur optik truber medien," *Ann. Phys.*, Vol. 25, pp. 377–44 5, 1908.

7. "Introduction to LIGO & gravitational waves." http://www.ligo.org/science/GW-Enhance.php. Accessed: 2016-11-02.

8. A. Abramovici et al., "LIGO: The Laser Interferometer Gravitational-Wave Observatory," *Science*, Vol. 256, No. 5055, pp. 325-333, Apr. 1992.

9. G. A. –Camelia, "Gravity-wave interferometers as quantum-gravity detectors," *N ature*, Vol. 398, No. 6724, pp. 216-218, Mar. 1999.

10. K. Srinivasan, P. E. Barclay, O. Painter, J. Chen, A. Y. Cho, and C. Gmachl, "Experimental demonstration of a high quality factor photonic crystal microcavit y," *Appl. Phys. Lett.*, Vol. 83, pp. 1915, 2003.

11. P.-T. Lee, T.-W. Lu, F.-M. Tsai, and T.-C. Lu, "Investigation of whispering gallery mode dependence on cavity geometry of quasiperiodic photonic crystal m icrocavity lasers," *Appl. Phys. Lett*., Vol. 89, 231111, 2006.

12. P.-T. Lee, T.-W. Lu, J.-H. Fan, and F.-M. Tsai, "High quality factor microcavity lasers realized by circular photonic crystal with isotropic photonic band gap effec t," *Appl. Phys. Lett*. Vol. 90, 151125, 2007.

13. F. Vollmer, S. Arnold, and D. Keng, "Single virus detection from the reactive shi ft of a whispering gallery mode," *PNAS*, Vol. 105, No. 52, pp. 20701, Dec. 2008.

14. S. M. Spillane, T. J. Kippenberg, and K. J. Vahala, "Ultralow-threshold Raman la ser using a spherical dielectric microcavity", *Lett. Nature*, Vol. 415, pp. 621-623,

Feb. 2002.

15. J. M. Gerard, B. Sermage, B. Gayral, B. Legrand, E. Costard, and V. Thierry-Mieg, “Enhanced Spontaneous Emission by Quantum Boxes in a Monolithic Optical Microcavity,” *Phys. Rev. Lett*. Vol. 81, 1110, 1998.

16. A. Lee, T. Mills, and Y. Xu, “Nanoscale welding aerosol sensing based on whispering gallery modes in a cylindrical silica resonator”, Optics Express, Vol. 23, No. 6, pp 7351-7365, Mar. 2015.

17. Y. Kokubun, in: Photonics Based on Wavelength Integration and Manipulation, IPAP Books 2 (IPAP, Tokyo, 2005), pp. 303–316.

18. D. G. Rabus, Integrated Ring Resonators: The Compendium (Springer, Berlin, 2007).

19. K. Djordjev, S.-J. Choi, S.-J. Choi, and P. D. Dapkus, “Microdisk tunable resonant filters and switches,” *IEEE Photon. Technol. Lett*. Vol. 14, No. 6, pp. 828-830, 2002.

20. M. Borselli, K. Srinivasan, P. E. Barclay, and O. Painter, “Rayleigh scattering, mode coupling, and optical loss in silicon microdisks,” *Appl. Phys. Lett.*, Vol. 85, pp. 3693, 2004.

21. T. J. Kippenberg, S. M. Spillane, and K. J. Vahala, “Kerr-Nonlinearity Optical Parametric Oscillation in an Ultrahigh-Q Toroid Microcavity,” *Phys. Rev. Lett.*, Vol. 93, 083904, 2004.

22. M. Hossein-Zadeh and K. J. Vahala, “Free ultra-high-Q microtoroid: a tool for designing photonic devices,” *Opt. Express*, Vol. 15, pp. 166-175, 2007.

23. P. Orlandi, C. Ferrari, M. John Strain, A. Canciamilla, F. Morichetti, M. Sorel, P. Bassi, and A. Melloni, “Reconfigurable silicon filter with continuous bandwidth tunability," *Opt. Lett.*, Vol. 37, No. 17, pp. 3669-3671, 2012.

24. Y. Ding, M. Pu, L. Liu, J. Xu, C. Peucheret, X. Zhang, D. Huang, and H. Ou, “Bandwidth and wavelength-tunable optical bandpass filter based on silicon microring-MZI structure," *Opt. Express*, Vol. 19, No. 7, pp. 6462-6470, 2011.

25. M.-C. Tien, A. T. Ohta, K. Yu, S. L. Neale, and M. C. Wu, “Heterogeneous integration of InGaAsP microdisk laser on a silicon platform using optofluidic assembly," *Appl. Phys. A*, Vol. 95, No. 4, pp. 967-972, 2009.

26. S. McCall, A. Levi, R. Slusher, S. Pearton, and R. Logan, “Whispering-gallery mode microdisk lasers," *Appl. Phys. Lett.*, Vol. 60, pp. 289, 1992.

27. A. M. Armani and K. J. Vahala, "Heavy water detection using ultra-high-Q micro cavities," *Opt. Lett.*, Vol. 31, No. 12, pp. 1896-1898, June 2006.

28. G. Yang, I. M. White, and X. Fan, "An opto-fluidic ring resonator biosensor for t he detection of organophosphorus pesticides," *Sensors and Actuators B*, Vol. 133, pp. 105-112, Feb. 2008.

29. D. Wang, Z. Wang, A. Lee, L. C. Marr, J. Heflin, and Y. Xu, "Highly sensitive n ano-aerosol detection based on the whispering gallery mode in cylindrical optical fiber resonators," *Aerosol Science and Technology*, Available online, Sep. 2016.

30. H. Rokhsari, T. J. Kippenberg, T. Carmon, and K. J. Vahala, "Theoretical and ex perimental study of radiation pressure-induced mechanical oscillations (parametri c instability) in optical microcavities," *IEEE J. Sel. Top. Quantum Electron.*, Vol. 12, No. 1, pp. 96–107, 2006.

31. T. J. Kippenberg and K. J. Vahala, "Cavity opto-mechanics," *Opt. Express*, Vol. 15, No. 25, pp. 17172–17205 , 2007.

32. T. J. Kippenberg and K. J. Vahala, "Cavity optomechanics: Back-action at the me soscale," *Science*, Vol. 321, No. 5893, pp. 1172–1176, 2008.

33. J. Hofer, A. Schliesser, and T. J. Kippenberg, "Cavity optomechanics with ultrahi gh-Q crystalline microresonators," *Phys. Rev. A*, Vol. 82, No. 3, 031804, 2010.

34. S. Tallur, S. Sridaran, and S. A. Bhave, "A monolithic radiation-pressure driven, l ow phase noise silicon nitride opto-mechanical oscillator," *Opt. Express*, Vol. 19 No. 24, pp. 24522–24529, 2011.

35. A. Cho, "Putting light's light touch to work as optics meets mechanics," *Scienc e*, Vol. 328, 5980, pp. 812–813, 2010.

36. D. Psaltis, S. R. Quake, and C. Yang, "Developing optofluidic technology throug h the fusion of microfluidics and optics," *Nature*, Vol. 442, No. 7101, pp. 381–38 6, 2006.

37. U. Levy and R. Shamai, "Tunable optofluidic devices," *Microfluid Nanofluidic s*, Vol. 4, pp. 97–105, 2008.

38. C. Monat, P. Domachuk, and B. J. Eggleton, "Integrated optofluidics: A new rive r of light," *Nat. Photonics*, Vol. 1, No. 2, pp. 106–114, 2007.

39. S.-H. Kim, J.-H. Choi, S.-K. Lee, S.-H. Kim, S.-M. Yang, Y.-H. Lee, C. Seassal, P. Regrency, and P. Viktorovitch, "Optofluidic integration of a photonic crystal n anolaser," *Opt. Express*, Vol. 16 No. 9, pp. 6515–6527, 2008.

40. Z. Li and D. Psaltis, "Optofluidic dye lasers," *Microfluid Nanofluidics*, Vol. 4, pp. 145–158, 2007.

41. H. Zhu, I. M. White, J. D. Suter, P. S. Dale, and X. Fan, "Analysis of biomolecul e detection with optofluidic ring resonator sensors," *Opt. Expres s*, Vol. 15, No. 15, pp. 9139–9146, 2008.

42. A. Ashkin and J. M. Dziedzic, "Radiation pressure on a free liquid surface," *Phys. Rev. Lett.*, Vol. 30, No. 4, pp. 139–142, 1973.

43. I. I. Komissarovak, G. V. Ostrovskaya, and E. N. Shedova, "Light pressure induc ed deformations of a free liquid surface," *Opt. Comm.* Vol. 66, No. 1, pp. 15–20, 1988.

44. J.-Z. Zhang and R. K. Chang, "Shape distortion of a single water droplet by laser-induced electrostriction," *Opt. Lett.* Vol. 13, No. 10, pp. 916–918, 1988.

45. H. M. Lai, P. T. Leung, K. L. Poon, and K. Young, "Electrostrictive distortion of a micrometer-sized droplet by a laser pulse," *J. Opt. Soc. Am. B*, Vol. 6, No. 12, pp. 2430–2437, 1989.

46. A. Casner and J.-P. Delville, "Adaptative lensing driven by the radiation pressure of a continuous-wave laser wave upon a near-critical liquid liquid interface," *Opt. Lett.*, Vol. 26, No. 18, pp. 1418–1420, 2001.

47. A. Casner, J.-P. Delville, and I. Brevik, "Asymmetric optical radiation pressure ef fects on liquid interfaces under intense illumination," *J. Opt. Soc. Am. B*, Vol. 20, No. 11, pp. 2355–2362, 2003.

48. M. Hossein-Zadeh and K. J. Vahala, "Fiber-taper coupling to Whispering-Gallery modes of fluidic resonators embedded in a liquid medium," *Opt. Expres s*, Vol. 14, No. 22, pp. 10800–10810, 2006.

49. A. Jonáš, Y. Karadag, M. Mestre, and A. Kiraz, "Probing of ultrahigh optical Q-f actors of individual liquid microdroplets on superhydrophobic surfaces using tape red optical fiber waveguides," *J. Opt. Soc. Am.*, Vol. 29, No. 12, pp. 3240–3247, 2012.

50. R. Dahan, L. L. Martin, and T .Carmon, "Droplet optomechanics," *Optica*, Vol. 3, No. 2, pp. 175-178, Feb. 2016.

51. S. Maayani, L. L. Martin, and T. Carmon, "Water-walled microfluidics for high-o ptical finesse cavities," *Nat. Comm.*, Vol. 7, No. 10, pp. 435, Jan. 2016.

Chapter 2

WGM Research Background

2.1 Optical losses, Quality factors

Due to practical limitations such as material absorption and surface scattering, optical energy stored within a resonator inevitably decreases over time. Suppose that the optical energy stored in the resonator decays over a time scale of τ, we can quantify the quality of the optical resonator using a quality factor, which can be defined as

$$Q = \omega_0 \frac{E_{stored}}{P_{loss}} = \omega_0 \tau = \frac{\lambda_0}{\Delta\lambda_{FWHM}} \tag{2.1}$$

where $\omega_0 = 2\pi f$ is angular frequency, λ_0 is the resonance wavelength in free space, τ is the ring-down lifetime (or photon storage time), and $\Delta\lambda_{FWHM}$ is the full-width at half-maximum of the resonance peak or dip in the wavelength domain. Given this definition, the *Q*-factor measures the characteristic time for the exponential decay of the energy stored inside the resonator. Therefore, higher *Q* suggests a longer storage time for optical energy circulating within the resonator. Alternatively, the *Q*-factor can be interpreted as the total energy of the circulating modes inside the resonator at equilibrium divided by the loss of energy (being absorbed by resonator material or dissipates) during one full oscillation period.

The loss of WGM resonator system can come from several sources including material absorption of resonator, surface scattering with non-ideal surface roughness, and optical field radiation from a resonator, and taper-resonator coupling. The *Q*-factor

associated with each loss factor can be represented by Q_{abs} , Q_{ss} , Q_{rad} , and Q_{coup} , respectively, where the total (or loaded) Q is deduced from all of these as follows,

$$\frac{1}{Q} = \frac{1}{Q_{abs}} + \frac{1}{Q_{ss}} + \frac{1}{Q_{rad}} + \frac{1}{Q_{coup}}. \tag{2.2}$$

In many WGRs, one of the most dominant loss factors is material absorption. The corresponding absorption limited Q (Q_{abs}) factor is given by

$$Q_{abs} = \frac{2\pi n_{eff}}{\alpha\lambda} \tag{2.3}$$

where n_{eff} and α represent the effective refractive index of the resonator and the absorption coefficient of resonator material (including a small contribution from Rayleigh scattering as well) at wavelength λ , respectively. In experiment, it is, therefore, important to use appropriate material for resonator fabrication at a given laser wavelength.

Scattering of light at residual surface inhomogeneity [1] can also cause loss in a resonator. The Q-factor limited by surface scattering (Q_{ss}) is given by [2]

$$Q_{ss} = \frac{3\varepsilon(\varepsilon+2)^2 \lambda^{3.5} D^{0.5}}{4\pi^3(\varepsilon-1)^{2.5}\sigma^2 B^2} \tag{2.4}$$

where ε is the permittivity of the medium, D is the diameter of resonator, σ is the RMS value of surface roughness, and B is the correlation length of surface inhomogeneity. Usually the scattering limited Q is assumed to be several orders of magnitude higher than other types of Q-factors because there is little of scattering in micro-resonators from highly controlled fabrication. In addition, a fluidic resonator, such as a liquid droplet, maintains its spherical shape by surface tension and thus the surface is atomically smooth.

For these resonators with very small surface roughness, we often omit Q_{ss} from total Q factor calculation.

The quality factor associated with the radiation loss Q_{rad} is given by [3]:

$$Q_{rad} = \frac{l^2 n_{core}}{k^3 c\varepsilon_0 N_s^2 n_{clad}^2 R^5 Z_0} \left[\begin{array}{l} n_{clad}\left(\frac{\pi}{\gamma_1}\right)^{0.25} j_l\left(kn_{core}R\right) j_{l+1}\left(kn_{clad}R\right) \\ -n_{core}\left(\frac{\pi}{\gamma_2}\right)^{0.25} j_{l-1}\left(kn_{core}R\right) j_l\left(kn_{clad}R\right) \end{array} \right]^{-2}, \tag{2.5}$$

$$\begin{aligned} \gamma_1 &= l - \frac{1}{2} - kn_{clad}R\frac{j_l\left(kn_{clad}R\right)}{j_{l-1}\left(kn_{clad}R\right)} + \frac{\left(kn_{clad}R\right)^2}{l} \\ \gamma_2 &= l + \frac{1}{2} - kn_{clad}R\frac{j_{l+1}\left(kn_{clad}R\right)}{j_l\left(kn_{clad}R\right)} + \frac{\left(kn_{clad}R\right)^2}{l} \end{aligned}, \tag{2.6}$$

$$N_s = \left\{ \sqrt{\frac{\pi}{m}} 2^{N-1} N!\, R^2 \left[\left(1 + \frac{1}{\alpha_s R}\right) j_l^2\left(kn_{core}R\right) - j_{l-1}\left(kn_{core}R\right) j_{l+1}\left(kn_{core}R\right) \right] \right\}^{-0.5}, \tag{2.7}$$

$$\alpha_s = \sqrt{\beta_l^2 - k^2 n_0^2}, \quad \beta_l = \frac{\sqrt{l\left(l+1\right)}}{R}, \quad N = l - m \tag{2.8}$$

where $Z_0 \simeq 377$ is the free space impedance. Often it is commonly assumed that resonators in air with diameter of $>100\mu m$ are assumed to be free from radiation loss [4]. However in a case where we design the index difference between the WGR and cladding medium smaller than ~0.1, even a resonator with several hundreds of micron can possess dominating radiation loss above all other loss mechanisms. Figure 2.1 shows an example of the radiation limited Q versus the diameter of micro-resonator.

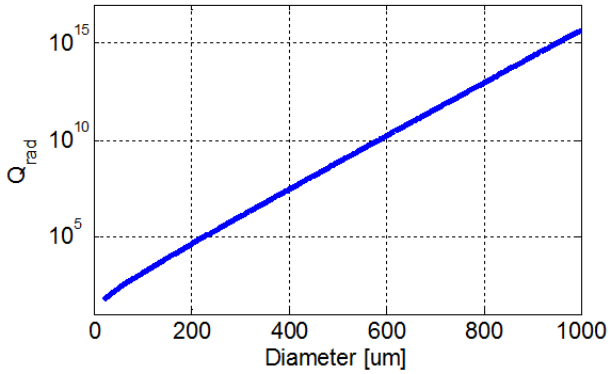

Figure 2.1. Radiation limited *Q*-factor at different resonator diameters.
(index contrast $\Delta n = n_{core} - n_{clad} = 0.027$)

Also the *Q*-factor associated with losses due to external coupling (Q_{coup}) can be approximated as [3],

$$Q_{coup} = \frac{2m\pi}{\kappa^2} \tag{2.9}$$

where κ is the WGM coupling coefficient and m is the azimuthal order of a WGM. Strong coupling between a WGR and a taper can introduce a loss of WGM power that depends on the coupling condition, e.g. taper-resonator gap distance. Unlike the other types of (intrinsic) *Q*-factors discussed above which are limited by the intrinsic property of resonator itself, Q_{coup} is sometimes called as an external *Q*-factor.

2.2 Finesse, Free spectral range

Finesse is one important parameter of WGRs. For many applications that require accurate measurements of resonance locations, higher finesse is often highly desirable. It is defined as the ratio of linewidth of the resonance and the free spectral range (FSR), which can be expressed as:

$$F = \frac{\Delta\lambda_{FSR}}{\Delta\lambda_{FWHM}} = Q\frac{\Delta\lambda_{FSR}}{\lambda} < Q\,. \tag{2.10}$$

In a WGM transmission spectrum, two successive resonances at azimuthal mode of order m and m+1 can be calculated as follow,

$$\lambda_{res,m} = \frac{2\pi na}{m}, \quad \lambda_{res,m+1} = \frac{2\pi na}{m+1} \tag{2.11}$$

where n and a are refractive index and radius of a resonator, respectively. Then a FSR which is the spacing between these two consecutive resonances can be estimated by

$$FSR = \lambda_{res,m} - \lambda_{res,m+1} = \frac{\lambda_{res,m}\cdot\lambda_{res,m+1}}{2\pi na} \simeq \frac{\lambda_{res,m}^2}{2\pi na} \tag{2.12}$$

where the approximation is valid as long as the circumference of the resonator is much greater than the resonance wavelength. While the FSR provides an absolute value of distance between the resonant peaks, the finesse provides the relative number of resonance linewidth that can fit inside the two consecutive resonances. A term ‘fully tunable resonator’ is occasionally used to denote a resonator whose resonant wavelength can be tuned over the entire FSR.

2.3 WGM Mode Numbers

A common geometry for WGM resonators is a sphere. In such a cavity, optical modes can be labelled using three mode numbers for the radial (n), azimuthal (m), and polar (l) dependences. The radial mode number n (=1, 2, ...) denotes the number of field maxima along the radial direction where the mode pattern is described by a spherical Bessel function. The polar mode number l (=1, 2, ...) roughly equals the number of wavelengths that can fit into the optical length of the equator, with 2l corresponds to the number of

field maxima in the azimuthal variation of the resonant field around the equator. The azimuthal mode number m (=-l, ..., +l) is the number of field maxima in the equator plane. Then $l - m + 1$ represents the number of field maxima in the polar direction. For a WGM with a smaller azimuthal mode index and a larger polar mode index, the peak of the WGM intensity will be pushed toward the equator of the resonator surface. A specific mode where $n = 1$ and $m = l \gg 1$ is called a fundamental mode that possesses the smallest mode volume and is highly preferred in many applications, e.g. ultra-low threshold lasers [5] due to the strongly focused field intensity at the circumference of WGR.

2.4 WGM Coupling

The modes in the WGR are strongly confined inside its surface by total internal reflection. As a result, direct access by a focused or collimated free-space beam is often very difficult. In practice, high efficiency WGM coupling is often achieved using near-field couplers. Many techniques have been developed to excite the optical modes in WGM resonators. Among existing methods, evanescent coupling through a fiber taper is one of the most promising approaches for distant (non-contact) coupling. In existing literature, evanescent coupling can be achieved using prism coupler [6], half block [7, 8], angle-polished fiber [9], and tapered fiber couplers.

For practical applications, efficient and controllable coupling of light to and from the WGR is important. There are two important parameters describing the coupling performance: efficiency (the ratio of power actually transferred to the resonator and total input power) and ideality (the ratio of the power transferred to the desired excitation

mode and the total power transferred to the resonator) [10]. Given these parameters, tapered fiber method shown in Fig.2.2 is widely used in many recent studies due to its advantages of high efficiency (efficiency nearly 100%, critical coupling) and easy alignment with a resonator. The evanescent coupling occurs when we bring a tapered fiber to the vicinity of the resonator, so that the evanescent fields of the resonator and the tapered fiber overlap significantly, thus enabling the tunneling of the optical wave from the tapered fiber to the resonator. In addition to the high efficiency, high ideality can also be an advantage of the taper based evanescent coupling. The tapered fiber based coupling method also allows simple focusing and alignment of the input optical power as well as the collection of output power that can be measured by a photodetector and used for the characterization of coupled WGMs.

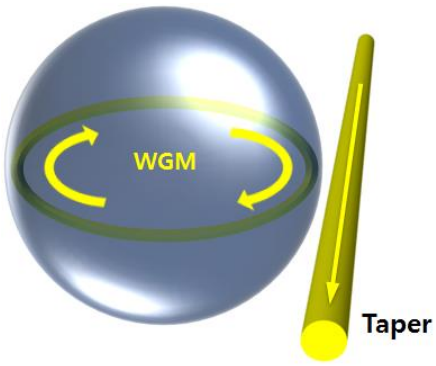

Figure 2.2. Evanescent coupling achieved using a tapered optical fiber positioned at the vicinity of a spherical WGR.

Another advantage of using tapered fiber is its relatively small size ($D < 1\mu m$) compared to other methods such that the space between coupler and resonator is visually accessible. In that condition, the amount of coupling can be adjusted by manipulating the gap distance between tapered fiber and resonator. This allows us to access different coupling regimes [11].

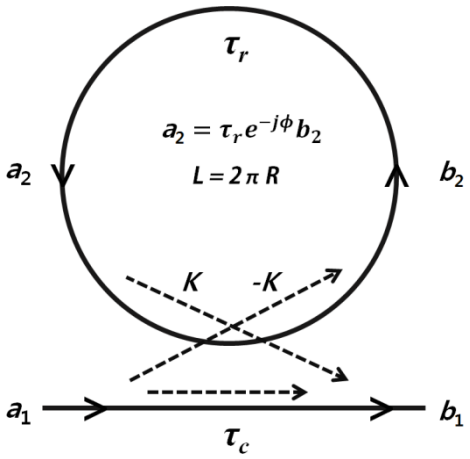

Figure 2.3. A diagram of WGM coupling described by coupling (κ) and transmission coefficients (τ_c), and a round-trip loss factor (τ_r).

The coupling between the tapered fiber and the WGM can be analyzed using the method in Fig. 2.3. Specifically, the input / output relationship between the electric field intensity after and before taper-resonator coupling (Fig. 2.3) is given by [12]

$$\begin{vmatrix} b_1 \\ b_2 \end{vmatrix} = \begin{vmatrix} \tau_c & \kappa \\ -\kappa & \tau_c \end{vmatrix} \begin{vmatrix} a_1 \\ a_2 \end{vmatrix} \tag{2.13}$$

where

$$|\tau_c|^2 + |\kappa|^2 = 1 . \tag{2.14}$$

Here, τ_c, κ, τ_r are the coefficients for throughput coupling, cross-over coupling, and the net transmission after one round trip in the resonator, respectively. Changing the coupling gap distance will modify τ_c, κ. Depending on the values of τ_c and κ, we can classify taper-resonator coupling into three distinct regimes.

(1) Under-coupled regime ($|\tau_r| < |\tau_c|$), where intrinsic losses of the cavity is larger than taper-resonator coupling.

(2) Critically-coupled regime ($|\tau_r| = |\tau_c|$): the intrinsic loss of cavity is equal to the strength of taper-resonator coupling. For this case, the magnitude of electric field coupled back into the taper is equal to the one transmitted through taper but they are out of phase. As a result, total transmission through the fiber taper becomes zero.

(3) Over-coupled regime ($|\tau_r| > |\tau_c|$): taper-resonator coupling is stronger than the intrinsic loss of the resonator.

Different transmission spectra associated with different taper-resonator coupling regimes are shown in Fig 2.4. It is worth to note that as the coupling condition switches from under-coupling to over-coupling (increase in κ), the rate of optical power coupled back from resonator to the waveguide increases as well and results in a higher loss. Thus it is shown in Fig. 2.4 that the WGM resonance in the under-coupling regime tends to possess a narrower linewidth and therefore a higher *Q* factor.

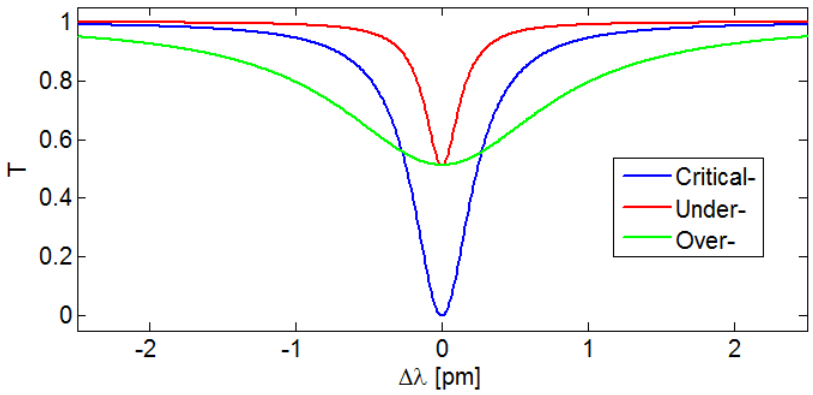

Figure 2.4. WGM resonance shapes in different coupling regimes.
(blue: critical coupling, red: under-coupling, green: over-coupling)

References

1. M. L. Gorodetsky, A. D. Pryamikov, and V. S. Ilchenko, “Rayleigh scattering in high-Q microsphereres,” *J. Opt. Soc. Am. B – Optical Physics*, Vol. 17, No. 6, pp. 1051-1057, 2000.

2. D. W. Vernooy, et al., “High-Q measurements of fused-silica microspheres in the near infrared,” *Opt. Lett.*, Vol. 23, pp. 247-249, 1998.

3. B. E. Little, J.-P. Laine, H. A. Haus, and L. Fellow, “Analytic theory of coupling from tapered fibers and half-blocks into microsphere resonators,” *J. Lightwave Technol.*, Vol. 17, No. 4, pp. 704-715, 1999.

4. J. R. Buck and H. J. Kimble, “Optimal sizes of dielectric microspheres for cavity QED with strong coupling,” *Phys. Rev. A*, Vol. 67, No. 3, 2003.

5. S. M. Spillane, T. J. Kippenberg, and K. J. Vahala, "Ultralow-threshold Raman la ser using a spherical dielectric microcavity," *Lett. Nature*, Vol. 415, pp. 621-623, Feb. 2002.

6. Collot L., Lefevreseguin V., Brune M., Raimond J. M., and Haroche S., “Very Hi gh-Q Whispering-Gallery Mode Resonances Observed On Fused-Silica Microsph eres,” *Europhysics Letters*, Vol. 23, No. 5, pp. 327-334, 1993.

7. N. Dubreuil, J. C. Knight, D. K. Leventhal, V. Sandoghdar, J. Hare, and V. Lefev re, “Eroded monomode optical fiber for whispering-gallery mode excitation in fused-silica microspheres,” *Opt. Lett.*, Vol. 20, No. 8, pp. 813-815, 1995.

8. J. C. Knight, N. Dubreuil, V. Sandoghdar, J. Hare, V. L.-Sejun, J. M. Raimond, and S. Haroche, “Mapping Whispering-Gallery Modes In Microspheres With A Near-Field Probe,” *Opt. Lett.*, Vol. 20, No. 14, pp. 1515-1517, 1995.

9. V. S. Ilchenko, X. S. Yao, and L. Maleki, “Pigtailing the high-Q microsphere cav ity: a simple fiber coupler for optical whispering-gallery modes,” *Opt. Lett*., Vol. 24, No. 11, pp. 723-725, 1999.

10. M. Gomilsek, "Whispering gallery modes," *Univ. of Ljubljana*, 2011.

11. M. Cai, O. Painter, and K. J. Vahala, “Observation of critical coupling in a fiber t aper to a silica-microsphere whispering-gallery mode system,” Phys. Rev. Lett., Vol. 85, No. 1, pp. 74-77, 2000.

12. A. Yariv, “Critical Coupling and Its Control in Optical Waveguide-Ring Resonat or Systems,” *IEEE Photonics Technology Lett.*, Vol. 14, No. 4, April 2002.

Chapter 3

Theoretical Background

3.1 Whispering Gallery Mode

3.1.1 Equations of WGMs in Spherical Resonators

To investigate the optical modes in a spherical resonator, we first start with Maxwell's equations:

$$\nabla \cdot \vec{D} = 0 \tag{3.1}$$

$$\nabla \cdot \vec{B} = 0 \tag{3.2}$$

$$\nabla \times \vec{E} = -\frac{\partial \vec{B}}{\partial t} = -\mu \frac{\partial \vec{H}}{\partial t} \tag{3.3}$$

$$\nabla \times \vec{H} = -\frac{\partial \vec{D}}{\partial t} = -\varepsilon \frac{\partial \vec{E}}{\partial t} \tag{3.4}$$

From the curl of Eq. (3.3) and using vector identity given as

$$\nabla \times \nabla \times \vec{A} = \nabla\left(\nabla \cdot \vec{A}\right) - \nabla^2 \vec{A}, \tag{3.5}$$

we find

$$\nabla \times \left(\nabla \times \vec{E}\right) = \nabla\left(\nabla \cdot \vec{E}\right) - \nabla^2 \vec{E} = -\mu \nabla \times \frac{\partial \vec{H}}{\partial t}. \tag{3.6}$$

Combining this with other Maxwell's equations and assuming a time-varying electric field $\vec{E}(\vec{r},t) = \vec{E}(\vec{r}) \cdot e^{i\omega t}$, we obtain

$$\nabla^2 \vec{E} + k^2 \vec{E} = 0, \quad \left(k = \omega\sqrt{\mu\varepsilon}\right) \tag{3.7}$$

Replacing $\vec{E}$ with $\vec{\psi}$ which represents either electric or magnetic field, we have

$$\nabla^2\vec{\psi} + k^2\vec{\psi} = 0 \tag{3.8}$$

and solutions to this equation in spherical coordinate is presented elsewhere [1]. Considering a transverse electric (TE) mode in which an electric field is parallel to the surface, the azimuthal and radial components of electric field are set to be zero. The only non-zero electric field component is E_θ which can be expressed as:

$$E_\theta = \psi(r,\theta,\varphi) = \psi_r(r)\cdot\psi_\theta(\theta)\cdot\psi_\varphi(\varphi) \tag{3.9}$$

Similar process can be used to study the transverse magnetic (TM) mode. ψ_r, ψ_θ, and ψ_φ represent the radial, polar, and azimuthal dependence of the field, respectively.

Expanding the wave equation (Eq. (3.7)) in spherical coordinate,

$$\frac{1}{r^2}\frac{\partial}{\partial r}\left(r^2\frac{\partial E}{\partial r}\right) + \frac{1}{r^2\sin\theta}\frac{\partial}{\partial r}\left(\sin\theta\frac{\partial E}{\partial \theta}\right) + \frac{1}{r^2\sin^2\theta}\frac{\partial^2 E}{\partial \varphi^2} + k^2 E = 0 \tag{3.10}$$

and using separation of variables, we obtain

$$\frac{1}{\psi_r}\frac{\partial}{\partial r}\left(r^2\frac{\partial \psi_r}{\partial r}\right) + \frac{1}{\psi_\theta\sin\theta}\frac{\partial}{\partial r}\left(\sin\theta\frac{\partial \psi_\theta}{\partial \theta}\right) + \frac{1}{\psi_\varphi\sin^2\theta}\frac{\partial^2\psi_\varphi}{\partial \varphi^2} = -k^2r^2 \tag{3.11}$$

where it can represent three ordinary differential equations in r, θ, and φ, respectively.

3.1.2 Radial, Azimuthal, Polar Dependence of Fields

(1) The radial dependence ψ_r is given by,

$$\psi_r(r) = \begin{cases} C_1\cdot j_l(kr) & (r < R_0) \\ C_2\cdot h_l(kr) & (r > R_0) \end{cases}, \tag{3.12}$$

where j_l is the spherical Bessel function of the first kind, h_l is the spherical Hankel function of the first kind, and R_0 is the radius of the spherical resonator. C_1 and C_2 are constants to be determined by the boundary condition at surface and the normalization condition. Fig. 3.1 shows the radial dependence of the electric field of a fundamental TE mode in a microsphere with refractive index $n_{core} = 1.45$, $\lambda = 735.55nm$, l = 758, and diameter $D = 125\mu m$, where red-dashed line represents the surface boundary of the resonator. Note that the y-axis is normalized so that the electric field intensity at resonator surface becomes 1.

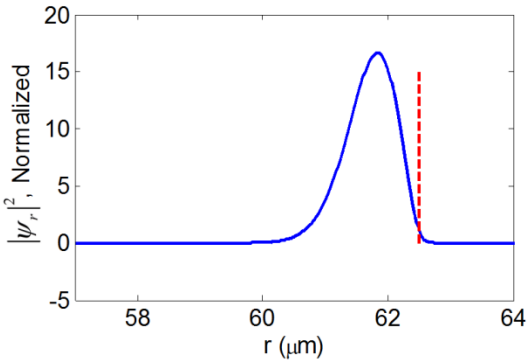

Figure 3.1. Radial dependence of WGM electric field profile ($R_0 = 62.5\mu m$, n_{core} = 1.45, λ = 735.55 nm, l = 758, n = 1).

An interesting observation is that a small fraction of the total optical power (i.e., the evanescent field) extends beyond the dielectric interface, with a total penetration depth of the order of $1\,\mu m$. This portion of optical power can interact with the cladding material. As a result, any change of the cladding medium can shift the resonance wavelength of the WGM in the resonator.

(2) Azimuthal dependence ψ_φ simply follows a sinusoidal oscillation as follows,

$$\psi_\varphi(\varphi) = \frac{1}{\sqrt{2}}\exp(im\varphi) \tag{3.13}$$

where it has a periodicity of 2π (equal phase after each revolution around the resonator) and the azimuthal mode number *m* is an integer. A constant $1/2\pi$ is chosen to have unity integral of $|\psi_\varphi|^2$ for one revolution.

(3) Lastly, the polar dependence ψ_θ is given by,

$$\psi_\theta(\theta) = N_\theta P_l^m(\cos\theta) \tag{3.14}$$

where $P_l^m(\cos\theta)$ is an associated Legendre polynomial and N_θ is a normalization constant to be chosen so that the integral of $|\psi_\theta|^2$ over θ is unity. A few examples of polar dependence of WGM field profile are shown in Fig. 3.2.

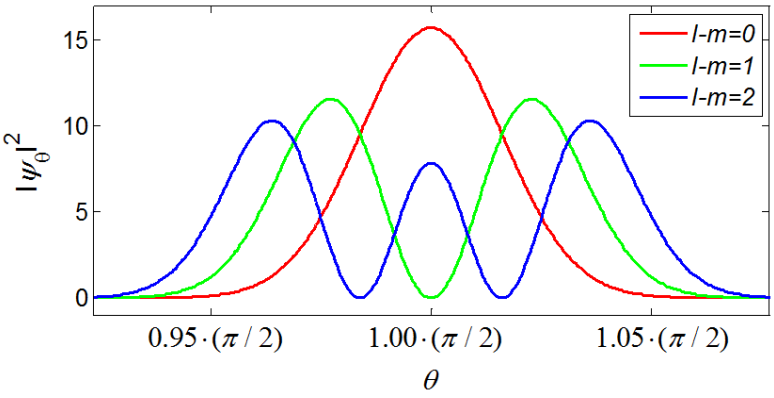

Figure 3.2. Polar dependence of WGM electric field profile.
(*l* = 775, red: *l*-*m*=0, green: *l*-*m*=1, blue: *l*-*m*=2)

3.2 Radiation Pressure

Electromagnetic (EM) wave propagating in space carries not only the energy, but it also carries a momentum. Therefore, an object placed within the path of an optical beam can experience an optical force, which is referred to as radiation pressure [2, 3]. Perhaps the

most intuitive way to imagine the radiation pressure is to consider a plane wave in free space.

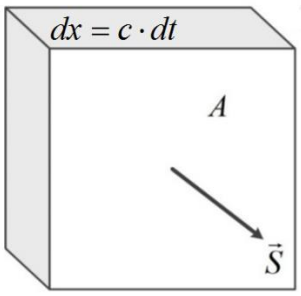

Figure 3.3. Plane wave passing through a volume element.
(*A*: surface area, *dx*: infinitesimal displacement of optical wave)

As a starting point, we consider a Poynting vector ($\vec{S}$) of an EM wave, defined as follows,

$$\vec{S} = \vec{E} \times \vec{H} \,. \tag{3.15}$$

Considering a uniform plane wave propagating along z-axis with its electric field polarized in x-direction, we have

$$\vec{E} = E_0 \cos(\omega t - kz)\hat{x} \tag{3.16}$$

and

$$\vec{H} = H_0 \cos(\omega t - kz)\hat{y} \,. \tag{3.17}$$

Then the Poynting vector is simply a cross product of these two fields and the resulted time-averaged expression is

$$< \vec{S} >= \frac{1}{2} E_0 H_0 \hat{z} = \frac{E_0^2}{2\eta_0} \hat{z} \tag{3.18}$$

where the factor of $1/2$ comes from the mean value of squared sinusoidal function and $\eta_0 = \sqrt{\mu_0 / \varepsilon_0} = 377\,\Omega$ is the intrinsic impedance of free space. In a case where a propagating EM wave impinges onto a perfectly absorbing object at normal angle, by the

law of momentum conservation, the momentum change of the object is $\Delta P = \Delta U / c$. Combining with the equations shown above, we find an expression of a radiation pressure vector as follows

$$\vec{P}_{rad} = \frac{\vec{F}}{A} = \frac{1}{A}\frac{d\vec{P}}{dt} = \frac{1}{c}\frac{d\vec{U}}{A \cdot dt} = \frac{<\vec{S}>}{c}. \tag{3.19}$$

For other cases involving with multiple dielectric materials with complex boundaries, we need to consider a general definition of optical force. For example, the electrostrictive force density $f(\bar{r})$ in a geometry of a spherical resonator can be expressed as [4]

$$f(\bar{r}) = \bar{f}_1 + \bar{f}_2 + \bar{f}_3 = \left[-\frac{1}{2}(\nabla\varepsilon)E^2\right] + \left[\frac{1}{2}(\nabla\gamma\varepsilon_0 E^2)\right] + \left[\varepsilon_0(\varepsilon_r - 1)\frac{\partial}{\partial t}(\bar{E}\times\bar{H})\right] \tag{3.20}$$

where E and H are the electric and magnetic fields, respectively, and ε is the electric permittivity as a function of radius r as follows

$$\varepsilon(\bar{r}) = \varepsilon_r(\bar{r}) \cdot \varepsilon_0 = \begin{cases} n^2\varepsilon_0, & r < R_0 \\ \varepsilon_0 & r > R_0 \end{cases} \tag{3.21}$$

with the refractive index of sphere n, a free-space permittivity ε_0, and $\gamma = (\varepsilon_r - 1) + (\varepsilon_r - 1)^2 / 3$. The first and second term in Eq. (3.20) are referred to as surface force density and volume force density, respectively, and at optical frequencies, the third term is negligible due to its time-averaged value converging to zero.

3.3 Fiber Bragg Grating

A fiber Bragg grating (FBG) typically refers to a fiber structure with spatially periodic index variations in the fiber core. When a broadband light is propagating through it, it selectively reflects only some of wavelengths that match the Bragg wavelength condition.

Since the FBG reflection peak depends on environmental conditions, FBGs have widely been used in temperature [5] and strain [6] sensing. In FBG based sensors, one can measure the wavelength associated with the FBG reflection peak (or transmission dip) in the spectral domain, thus the power fluctuation in light source does not significantly affect the accuracy of measurement. One approach for fabricating FBGs is to expose the germanium-doped silica fiber [7, 8] to a periodic pattern of intense ultraviolet (UV) beam. Under the UV exposure, the refractive index of fiber core increases permanently as much as the exposure time and intensity of UV beam. Figure 3.4 shows a schematic illustration of a FBG with a period of Λ and grating array length of L.

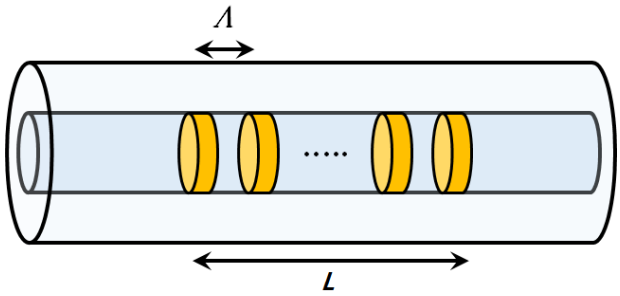

Figure 3.4. Schematic illustration of FBG with a grating period (Λ) and a length of grating array (L).

The Bragg wavelength (λ_B) associated with the FBG reflection peak can be estimated as,

$$\lambda_B = 2 \times n_{eff} \times \Lambda \tag{3.22}$$

where both the effective index (n_{eff}) of optical fiber and grating period (Λ) vary with the temperature changes. The FBG temperature sensing is based on the thermo-optic and thermal expansion coefficients of optical fiber. Here, the thermo-optic coefficient represents the change of refractive index by temperature and the thermal expansion

coefficient describes the linear expansion of grating period by temperature. Therefore, the approximate change of Bragg wavelength can be derived from

$$\frac{\partial \lambda_B}{\partial T} \simeq \lambda_{B,0} \cdot \left[\frac{1}{n} \frac{\partial n}{\partial T} + \frac{1}{\Lambda} \frac{\partial \Lambda}{\partial T} \right] = \lambda_{B,0} \cdot (\alpha_n + \alpha_\Lambda) \tag{3.23}$$

where $\lambda_{B,0}$ is the initial Bragg wavelength, α_n is the thermo-optic coefficient, and α_Λ is the linear thermal expansion coefficient. Based on Eq. (3.23), the magnitude of Bragg wavelength shift ($\Delta\lambda_B$) and the amount of temperature change can be related to each other as:

$$\Delta\lambda_B = \lambda_{B,0} \times \alpha_{therm} \times \Delta T \tag{3.24}$$

where the thermal coefficient (α_{therm}) of silica is a sum of the two coefficients ($\alpha_{therm} = \alpha_n + \alpha_\Lambda$). The thermal coefficient of FBG ($\alpha_{FBG} = \lambda_{B,0} \cdot \alpha_{therm}$) is limited by the intrinsic material property of fused silica which is typically on the order of 10 pm/^{o}C at 1530 nm. The linear relation between $\Delta\lambda_B$ and ΔT remains valid over a wide temperature range.

References

1. Y. Lan, "Fabrication and characterization of microlasers by the sol-gel mothod," *California Institute of Technology: PhD dissertation*, 2005.

2. A. Robinson, M. Zepf, S. Kar, R. G. Evans, and C. Bellei, “Radiation pressure ac celeration of thin foils with circularly polarized laser pulses,” *New J. of Phys.*, Vo l. 10, pp. 1-13, 2008.

3. A. Ashkin, “Acceleration and trapping of particles by radiation pressure,” *Phys. R ev. Lett.*, Vol. 24, No. 4, pp. 156-159, 1970.

4. H. M. Lai, *et al.*, "Electrostrictive distortion of a micrometer-sized droplet by a la ser pulse", *J. Opt. Soc. Am. B*, Vol. 6, No. 12, pp. 2430-2437, Dec. 1989.

5. D. Y. Wang, Y. Wang, J. Gong, and A. Wang, “Fully distributed fiber-optic temperature sensing using acoustically-induced rocking grating,” *Opt. Lett.*, Vol. 36, No. 17, pp. 3392-3394, 2011.

6. L. Ma, C. Ma, Y. Wang, D. Y. Wang, and A. Wang, “High-speed quasi-distributed strain sensing based on time division multiplexing of fibre Bragg grati ngs,” *Electronics Letters*, Vol. 52, No. 8, 2016.

7. G. Keiser, *Optical Fiber Communications, 4th edition*, (McGraw-Hill Education, 2010).

8. G. Meltz, W. W. Morey, and W. H. Glenn, “Formation of Bragg gratings in optic al fibers by a transverse holographic method,” *Opt. Lett*. Vol. 14, pp. 823-825, 19 89.

Chapter 4

Theoretical Analysis

4.1 Droplet Surface Deformation at Steady-state

In our previous analysis [1], we theoretically demonstrated that the radiation pressure of a WGM circulating within a liquid droplet can produce significant interfacial deformation. Our approach is based on solving the Young-Laplace equation, which states that under steady-state and at the droplet surface, the surface tension (σ), the pressure jump across the droplet interface (Δp), and WGM's radiation pressure (p_{rad}) must balance each other:

$$\Delta p + p_{rad} = \sigma \nabla \cdot \hat{n} \tag{4.1}$$

$$p_{rad} = \frac{1}{2}\varepsilon_0 (n_{core}^2 - n_{clad}^2)\left|\vec{E}_s\right|^2, \tag{4.2}$$

where σ is the interfacial tension at the droplet surface, $\hat{n}$ is the unit vector normal to the surface, ε_0 is the free space permittivity, n_{core} and n_{clad} are the refractive indices of the core and the cladding region, and $\left|\vec{E}_s\right|^2$ is the electric field of the WGM at the droplet surface. In Equation (4.1), the pressure jump Δp is a constant, and the pressure due to surface tension is $\sigma \nabla \cdot \hat{n}$. Throughout this study, we will use ΔR to represent the droplet deformation and R_0 to denote the original droplet radius. For a WGM circulating near the equator of the droplet, the deformed droplet should retain axial symmetry, and ΔR should be a function of θ only. Assuming small deformation (i.e., $\Delta R \ll R_0$), Eq. (4.1) can be converted to [2]:

$$\frac{d^2\Delta R}{d\theta^2}+\cot\theta\frac{d\Delta R}{d\theta}+2\Delta R=-\frac{R_0^2}{\sigma}(\Delta p+p_{rad}). \tag{4.3}$$

Eq. (4.3) can be solved numerically. The exact solution of the polar (θ) dependence of the deformed droplet is shown in Fig. 4.1 as blue curve. It is, however, more instructive to obtain a closed-form approximate solution by expanding $\Delta R(\theta)$ in terms of spherical harmonic function Y_{LM} as $\Delta R(\theta)=\sum_L\sqrt{4\pi}\Delta R_L Y_{L0}$, where ΔR_L is the expansion coefficient, and L must be a positive even integer, i.e., L = 2, 4, 6, ⋯. We have found that it is often sufficient to consider only the lowest order $L=2$ term. (For comparison, the θ dependence of Y_{20} is shown in Fig. 4.1 as the dashed red curve.)

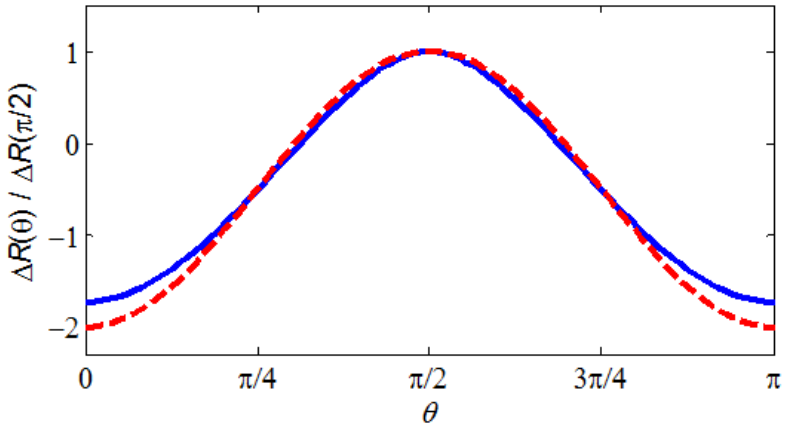

Figure 4.1. Polar dependence of droplet deformation.
(Blue solid line: exact solution, Red dashed line: L = 2 term only)

Next, consider a transverse electric (TE) WGM with polar mode number l and azimuthal mode number m, whose electric field is $\vec{E}_{lm}=g_l(r)\vec{X}_{lm}(\theta,\varphi)$. $\vec{X}_{lm}(\theta,\varphi)$ is the vector spherical harmonic function. If we only consider the lowest order droplet deformation ($L=2$), the maximum deformation occurs at the equator $\Delta R(\theta=\pi/2)$, and its magnitude, induced by the radiation pressure of the aforementioned TE WGM, can be expressed as [1]:

$$\Delta R(\theta = \pi/2) = \frac{\varepsilon_0 \lambda R_0}{4 n_{core}} (n_{core}^2 - n_{clad}^2) \frac{\Gamma_\theta^{lm}}{\Gamma_\sigma} \frac{\left|\vec{E}_s^{\max}\right|^2}{\sigma} \tag{4.4}$$

where $\vec{E}_s^{max}$ represents the maximum magnitude of $\vec{E}_{lm}$ on the surface of the droplet, Γ_θ^{lm} and Γ_σ are two dimensionless constant, with Γ_θ^{lm} typically varies in the range of 1 to 5, and Γ_σ is of the order of 1. Since the WGM power is always proportional to $\left|\vec{E}_s^{max}\right|^2$, Eq. (4.4) predicts that the radiation pressure induced surface deformation is always proportional to WGM power, and inversely proportional to the interfacial tension σ. To capture the essence of this physical insight, we re-write Eq. (4.4) as:

$$\Delta R / R_0 = P_{WGM} / P_{sat} \tag{4.5}$$

From now on, unless otherwise specified, ΔR always refers to droplet deformation at the equator, i.e., $\Delta R(\theta = \pi/2)$. In Eq. (4.5), we introduce a constant P_{sat}, which quantifies the strength of radiation pressure induced nonlinearity, and shall be referred to as saturation power. The physical meaning of P_{sat} is clear: it represents the power of the WGM required to increase the droplet radius by 100%. We can determine the value of P_{sat} by calculating ΔR induced by a WGM with $P_{WGM} = 1$ W.

4.2 Harmonic Oscillator (HO) Model

For a quantitative comparison between theory and experiment, we extend our previous steady-state analysis [1] to the following framework, where optical fields and liquid droplets are dynamically coupled together via radiation pressure. Following the analysis in [3], we use a harmonic oscillator (HO) model to phenomenologically describe how the droplet responds to radiation pressure. Taking into consideration of the axial symmetry of

the droplet geometry and the WGM energy distribution, the droplet interface deformation $\Delta R(t,\theta)$ and the radiation pressure distribution $F(t,\theta)$ can be expanded in Legendre series as,

$$\Delta R(t,\theta) = \sum_{L=2}^{\infty} \Delta R_L(t) P_L(\cos\theta) \tag{4.6}$$

$$F(t,\theta) = \sum_{L=2}^{\infty} F_L(t) P_L(\cos\theta) \tag{4.7}$$

where $P_L(\cos\theta)$ is the Legendre function, and L's are positive even numbers. The mechanical motion of the interface at different mode number L can then be described by the following differential equation,

$$\Delta\ddot{R}_L + 2\mu_L \Delta\dot{R}_L + \omega_L^2 \Delta R_L = \frac{L}{\rho R_0} F_L \tag{4.8}$$

where

$$\mu_L = \frac{\mu}{\rho R_0^2}(2L+1)(L-1) \tag{4.9}$$

and

$$\omega_L^2 = \frac{\sigma}{\rho R_0^3} L(L+2)(L-1)\,. \tag{4.10}$$

The derivation of the above expressions is available in Refs. [3-6] and is not repeated here. We find that with the material properties used in our system, the first five ($L = 2, 4, 6, 8, 10$) terms are under-damped and all $L > 10$ terms are over-damped [6]. For the five under-damped modes, damping ratios are found to be 0.29, 0.51, 6.68, 0.81, and 0.93, respectively. Because the mechanical mode $L = 2$ is less likely damped, we only

consider the leading term $L = 2$ in the following analysis of the droplet interfacial motion, and the subscript L will be dropped for a simplicity.

In order to simulate the transient droplet interface deformation, the forcing term in Eq. (4.8) is estimated as follows. With a given constant WGM power (P_{WGM}), the steady-state interface deformation ($\Delta R / R_0$) is computed following the analytical and numerical procedures proposed in [2]. The right-hand-side of Eq. (4.8) then becomes $\omega^2 R_0 (\Delta R / R_0)$. The droplet interface deformation at the equator (ΔR) is related to the saturation power (P_{sat}) and P_{WGM} by Eq. (4.4). Note that P_{sat} is constant and can be estimated by the interface deformation at a given P_{WGM} value. Now Equation (4.8) can therefore be re-written as

$$\Delta\ddot{R} + 2\mu\Delta\dot{R} + \omega^2 \Delta R = \omega^2 R_0 \frac{P_{WGM}}{P_{sat}} . \tag{4.11}$$

Typically it is difficult to accurately measure the interfacial tension between two different liquids. However, since P_{sat} is proportional to interfacial tension, we can easily determine the value of P_{sat} for different interfacial tensions. A major difference between our work and other's previous study is that P_{WGM} depends strongly on droplet deformation. In fact, for any given $\Delta R(t)$, we can relate the WGM power and the input power as

$$P_{WGM} = \frac{\tau_r^2 \kappa^2}{\left|\tau_r \tau_c - \exp(-i\phi(t))\right|^2} P_{in} \tag{4.12}$$

where $\phi(t)$, which represents total phase shift of one round trip, can be explicitly linked to $\Delta R(t)$ as

$$\phi(t) = 4\pi^2 n_{eff} \frac{1}{\lambda(t)} (R_0 + \Delta R(t)) \tag{4.13}$$

where n_{eff} is the effective index of the WGM and can be well approximated to be n_{core}. In our experiments, the laser wavelength ($\lambda(t)$) is scanned at a speed V_{scan} and can be estimated as

$$\lambda(t) = \lambda_0 + V_{scan} t \,. \tag{4.14}$$

The scan speed is in the range of 0.01 – 10 nm/s. Equations (4.11-4.14) govern the droplet interface motion induced by the radiation pressure under a given V_{scan}. The nonlinear ordinary differential equation (ODE, Eq. (4.11)) is solved numerically by the MATLAB ODE solver 'ode45'. The transmitted power can also be estimated by the relation,

$$P_{tran} = \frac{\left|\tau_r - \tau_c \exp(-i\phi(t))\right|^2}{\left|\tau_r \tau_c - \exp(-i\phi(t))\right|^2} P_{in} \,. \tag{4.15}$$

Strictly speaking, the HO model can only provide an approximate solution for the radiation pressure induced droplet deformation. However considering the droplet's near-spherical shape maintained by its surface tension and the small scale of deformation $\Delta R / R_0$, this HO model can offer a realistic description of our experiments. There may be some discrepancy when it comes to deal with an oscillatory behavior (e.g. extra damping by contact with solid, change of natural frequency), but further analyses for those of additional effects are over the scope of this manuscript and we simply assume it to be a minor experimental noise.

4.3 Linear Steady-state Estimation

We also use another simple estimation that can relate $\Delta\lambda_{res}$ and ΔP_{in}. First, estimate the time for the WGM to travel around the droplet, which is

$$\Delta t = 2\pi R / \left(c / n_{core} \right). \tag{4.16}$$

During this time, the total loss in optical energy within the droplet is

$$\Delta E_{WGM} = 2\pi\alpha R P_{WGM} \Delta t. \tag{4.17}$$

At the same time, we measure the optical power difference between the input and output of taper

$$\Delta P_{in} = P_{in} - P_{out}. \tag{4.18}$$

By equating the energy input from taper ($\Delta P_{in}\Delta t$) to the loss of WGM energy in Eq. (4.17), we have

$$\Delta P_{in} = 2\pi\alpha R P_{WGM}. \tag{4.19}$$

With a known relation

$$\frac{\Delta\lambda_{res}}{\lambda} = \frac{P_{WGM}}{P_{sat}}, \tag{4.20}$$

we find a direct estimation of WGM resonance shift driven by radiation pressure

$$\Delta\lambda_{res} = \frac{\Delta P_{in}\lambda}{2\pi\alpha R P_{sat}}. \tag{4.21}$$

References

1. Y. Xu, P. Zhang, S. Jung, and A. Lee, “Analysis of radiation pressure induced no nlinear optofluidics,” *Opt. Express*, Vol. 22, No. 23, Nov. 2014.

2. P. Zhang, S. Jung, A. Lee, and Y. Xu, “Radiation-pressure-induced nonlinearity i n microdroplets,” *Phys. Rev. E,* Vol. 92, 063033, 2015.

3. H. M. Lai, P. T. Leung, K. L. Poon, and K. Young, “Electrostrictive distortion of a micrometer-sized droplet by a laser pulse,” *J. Opt. Soc. Am. B,* Vol. 6, No. 12, pp. 2430-2437, 1989.

4. I. Brevik and R. Kluge, “Oscillations of a water droplet illuminated by a linearly polarized laser pulse,” *J. Opt. Soc. Am. B,* Vol. 16, No. 6, pp. 976-985, 1999.

5. S. A. Ellingsen, “Microdroplet oscillations during optical pulling,” *Phys. Fluids*, Vol. 24, 022002, 2012.

6. S. A. Ellingsen, “Theory of microdroplet and microbubble deformation by Gaussi an laser beam,” *J. Opt. Soc. Am. B*, Vol. 30, No. 6, pp. 1694-1710, 2013.

Chapter 5

Droplet WGM Experimental Configuration

5.1 Tapered Fiber Fabrication

The tapered fiber is fabricated using a heat-and-pull method [1, 2]. As shown in Fig. 5.1, a single mode fiber (SMF) or nearly SMF is fixed between two fiber clamps where each clamp is separately mounted on motorized linear stages (LSs) moving in opposite directions. We use a propane-oxygen torch to heat up the fiber to its softening temperature. A half-side cut silica tube is placed between the flame and clamped fiber to protect the sample from contaminants of gas combustion. Also the silica tube spreads the heat along the fiber to ensure uniform heating of the tapered section. The motorized linear stages are controlled by computer software where the pulling speed is optimized to achieve longer taper length with low transmission loss.

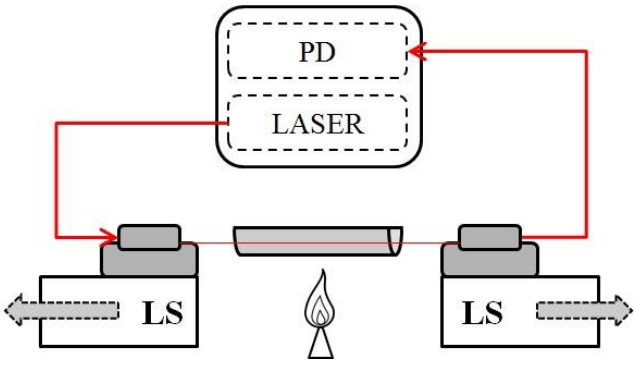

Figure 5.1. Schematic diagram of a taper fabrication system based on heat-and-pull method. (LS: linear stage, PD: photo-detector, red-arrows: optical fiber)

During the taper pulling process, the taper transmission fluctuates because the taper geometry changes and different optical modes propagating within the tapered

section interfere with each other. The pulling process is stopped when the transmission becomes stationary, where it implies that the tapered section is thin enough to meet the single-mode (SM) condition. An example of taper transmission during the taper pulling is shown in Fig. 5.2 where we use a near-single mode fiber (780HP, Thorlabs) at a laser wavelength of $\lambda = 729nm$.

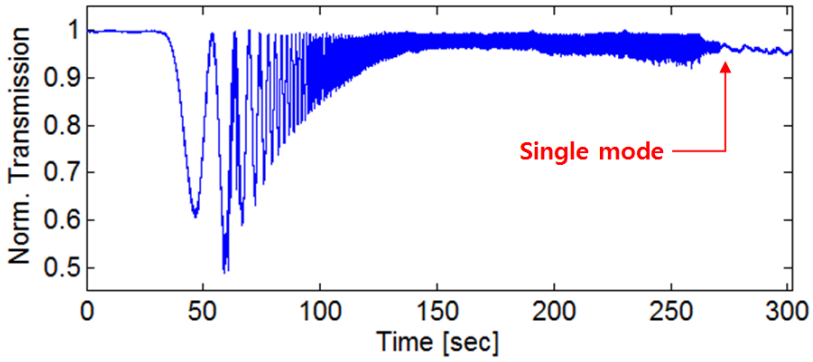

Figure 5.2. Taper transmission (λ = 729 nm) during the heat-and-pull process. Single-mode condition from ~270 sec (T > 95%). (Fiber preform: 780HP).

As the diameter of optical fiber decreases during the pulling process, there is a transition where the optical field in the fiber leaks out to the outer medium (air). After this transition, the air becomes a cladding of the waveguide and tapered fiber itself becomes a core made of silica rod. For such a simple waveguide, the single mode condition is given as,

$$D_{SM} = 2r_{sm} < \frac{2.405 \cdot \lambda}{\pi \sqrt{n_{core}^2 - n_{clad}^2}} \tag{5.1}$$

where n_{core} is typical refractive index of silica optical fiber ($n_{core} = 1.45$), n_{clad} is simply the index of air, and λ is the wavelength of propagating optical field. In our experiment, we use a tunable laser (TL) diode at $\lambda \sim 735\,nm$, and from Eq. (5.1), the taper diameter at SM is estimated to be $D_{SM,air} \sim 536nm$. For a SM taper fabrication, we usually start by

tuning the laser wavelength at the shortest value in the range so that, once the taper diameter exhibits SM operation, it will maintain SM operation at all other available wavelengths. At such a small diameter, the optical mode propagating along the taper reaches outer medium, i.e. air, in a range of several hundred nanometers away from the boundary and the overlap with the evanescent tail of droplet WGM will enable sufficient optical coupling. Both of the cross sectional mode patterns of tapered fiber ($D_{taper} = 500nm$) in air (left, $n_{clad} = 1$) and water (right, $n_{clad} = 1.33$) are shown in Fig. 5.3 in which the white dashed circle represents the circumference of tapered fiber.

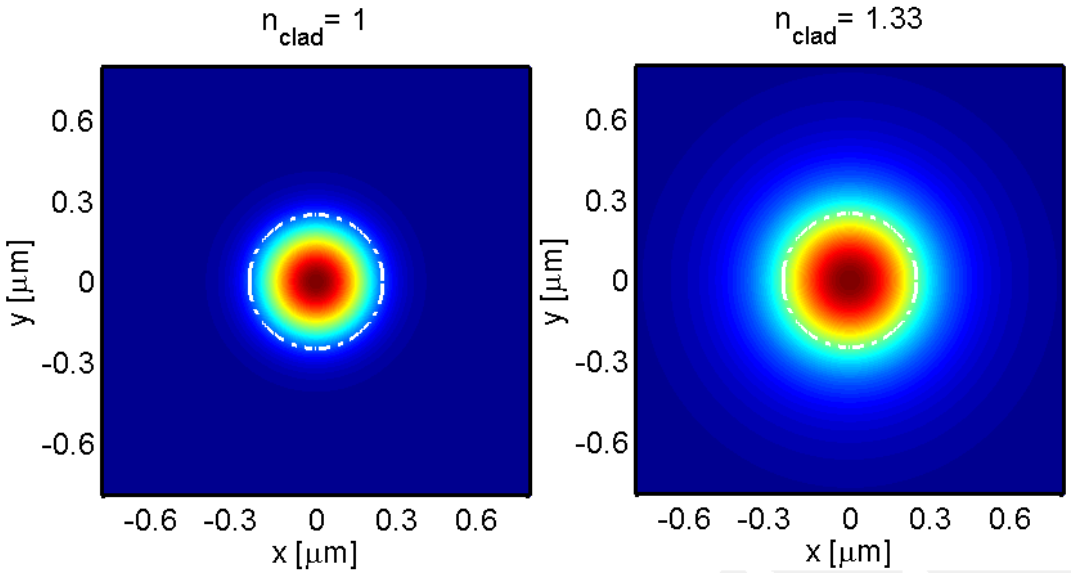

Figure 5.3. Mode patterns at the waist of tapered fiber in air (left, n_{clad} = 1) and water (right, n_{clad} = 1.33). (D = 500 nm, n_{core} = 1.45, λ = 735 nm).

The radial dependence of the optical wave guided in the fiber taper is shown in Fig. 5.4. Due to the lower index contrast, taper submerged in water exhibits longer evanescent tail. The SM taper fabricated in air operates in single mode as well as in water because the water medium requires larger single mode diameter ($D_{SM,water} \simeq 974nm$) than air.

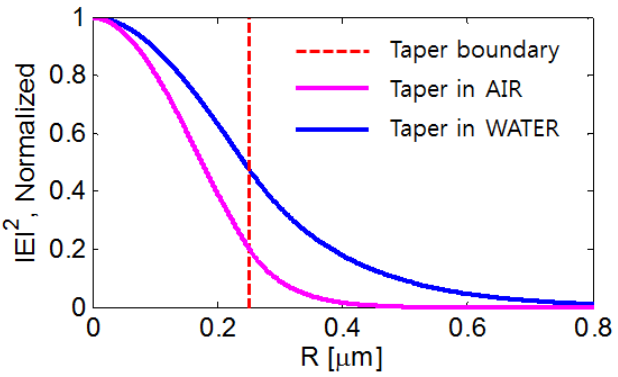

Figure 5.4. Radial dependence of taper mode pattern (R = 250 nm, λ = 735 nm).

Since the taper diameter at SM condition is extremely small and fragile, the sample must be fixed on a rigid holder that can maintain the structural integrity of taper. The taper holder is made of glass slide that is grinded in U-shape. After the taper fabrication step is done, we place the holder just below the taper and fix both input and output sides of taper onto the holder with epoxy as shown in Fig. 5.5. We have used this technique to transfer the taper sample into a water chamber without damaging the taper.

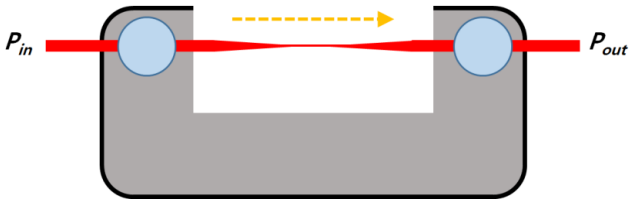

Figure 5.5. Schematic diagram of taper holder (taper in red).

5.2 Droplet Resonator

The high-Q resonator is a drop of index matching fluid ($n_{core} = 1.357$, diameter $D \simeq 500\mu m$) placed on a stem and submerged in water ($n_{clad} = 1.33$) as shown in Fig. 5.6.

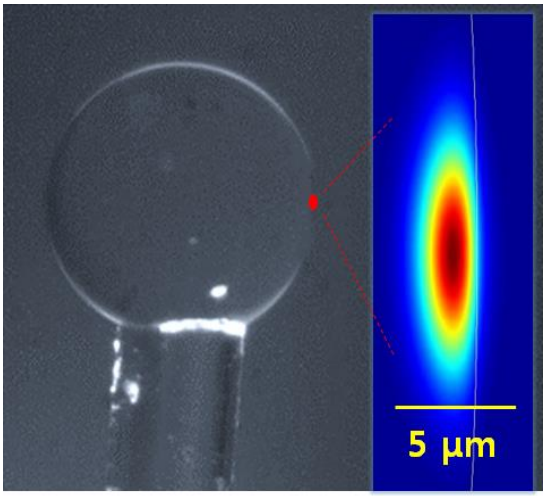

Figure 5.6. Image of a fluidic droplet resonator (left) and the WGM pattern in $r-\theta$ plane (right). Due to the low index contrast between droplet and water medium, the boundary of droplet vaguely appears in the image.

Firstly a support made of a standard optical fiber ($D=125\mu m$) with its end-face cleaved is glued vertically (using epoxy) onto the bottom of transparent water chamber ($10\,cm\times10\,cm\times3\,cm$). Then a syringe needle forms a droplet (Perfluorocarbon and Chlorofluorocarbon, AAA13600, Cargille) inside the water volume and we use a $80\mu m$ fiber-tip to capture the droplet and transfer it to the top of support. In this method, we were able to generate droplets with their diameters in a range of $300-1000\mu m$. Due to the interfacial tension and relatively large size of droplet compared to the diameter of support, the droplet maintains its near-spherical shape. Other optofluidic parameters of core and cladding liquid are listed in Table 5.1.

	α (m^{-1})	n	σ (mN/m)	μ (cSt)	ρ (kg/m^3)
Core	0.26	1.357	19	16	1917
Cladding	2	1.330	72	1	1000

Table 5.1. Optofluidic properties of core and cladding liquid.

The whole sample structure is built on a floated optical table (Newport, S-2000A-428) to isolate vibration transmitted from the lab environment. Also the water chamber containing a droplet resonator is covered by another external air chamber that blocks the air flow.

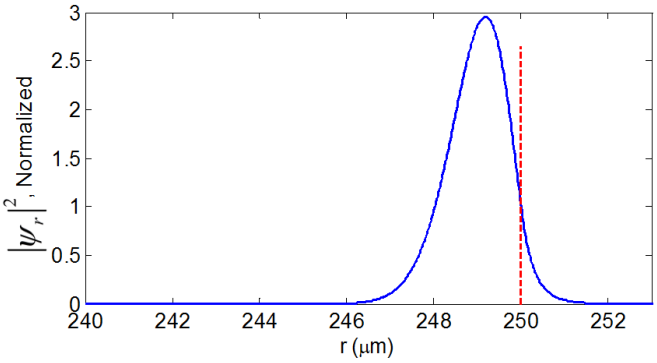

Figure 5.7. Radial dependence of droplet WGM electric field profile.
($R_0 = 250\mu m$, n_{core} = 1.375, n_{clad} = 1.330, $\lambda = 734.92$nm, l = 2880, n = 1)

Fig. 5.7 shows the radial dependence of a fundamental TE WGM in the droplet resonator with $\lambda = 734.92nm$, $l = 2880$, and a diameter $D = 500\mu m$, where the red-dashed line represent the surface of resonator. Note that the y-axis is normalized so that the electric field intensity at resonator surface becomes 1. The evanescent tail of electric field extends a few microns out of resonator interface. As a result, it is possible to achieve non-contact coupling with the optical signals in the tapered fiber, since there is significant overlap between the evanescent fields of the WGM and the fiber taper mode. The strength of WGM field confinement can be significantly changed by varying the index contrasts between the core and cladding medium. Figure 5.8 shows the length of evanescent field δ_p (or penetration depth) for a fundamental WGM in our resonator at various index contrasts in which

$$\left|E\left(r=\delta_p\right)\right| = \left|E\left(r=R_0\right)\right| \cdot e^{-1}. \tag{5.2}$$

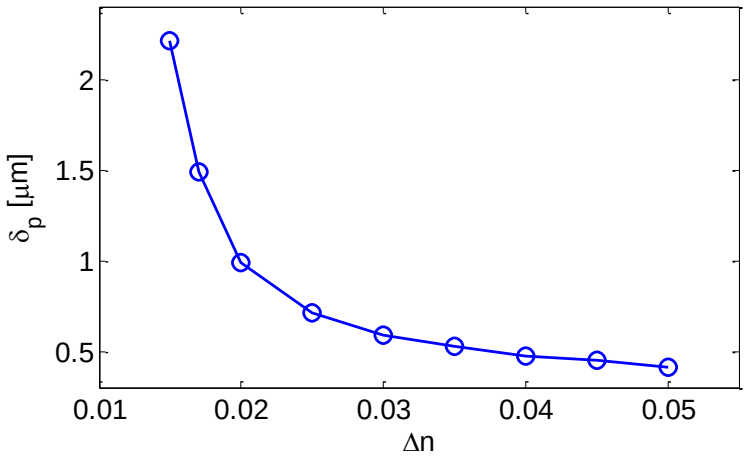

Figure 5.8. Penetration depth (length of evanescent field) of droplet WGM at different index contrasts (D = 500 μm, n_{clad} = 1.330).

Due to the attraction force (e.g. Van der Waals force) between the tapered fiber and droplet, we find that the position of fiber taper tends to drift toward the droplet surface when the gap distance d_{gap} between the two objects is too small (i.e. $d_{gap} < 500nm$). Maintaining certain gap of d_{gap} is one of the most important factors when dealing with fluidic WGM resonators because direct contact between the taper and droplet may deform the droplet shape (as well as the optical modes inside) and induce significant loss in taper transmission. Therefore, smaller index contrast is preferred for a successful non-contact WGM coupling. However as the index contrast between core and cladding decreases, the droplet can no longer effectively confine light near its interface. As the evanescent field reaches further outside of the resonator, the radiation loss of the WGM can increase significantly. Therefore, we choose the index contrast of droplet resonator to be sufficiently low such that the radiation limited Q factor remains higher than other types of Q-factors (e.g. Q_{abs}). The radiation limited Q-factors at different index contrasts are shown in Fig. 5.9. Finally from the two estimates of Fig. 5.8 and 5.9, we choose the

optimal index difference to be 0.027, where the fundamental WGM possesses ~660 nm penetration depth and its radiation limited Q factor is $Q_{rad} = 6.7 \times 10^8$.

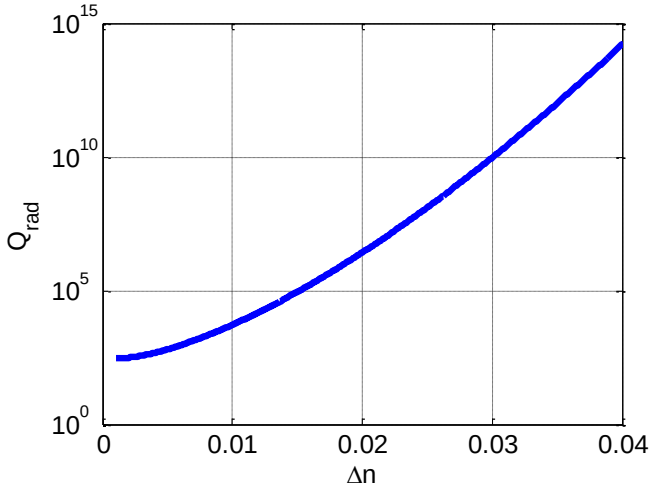

Figure 5.9. Radiation limited *Q*-factors at different index contrasts (D = 500μm, n_{clad} = 1.330)

In addition to the radial dependence of droplet WGM, the polar dependence is also shown in Fig. 5.10 assuming the azimuthal and polar mode orders are equal ($l = m$) and with all other parameters same as described above.

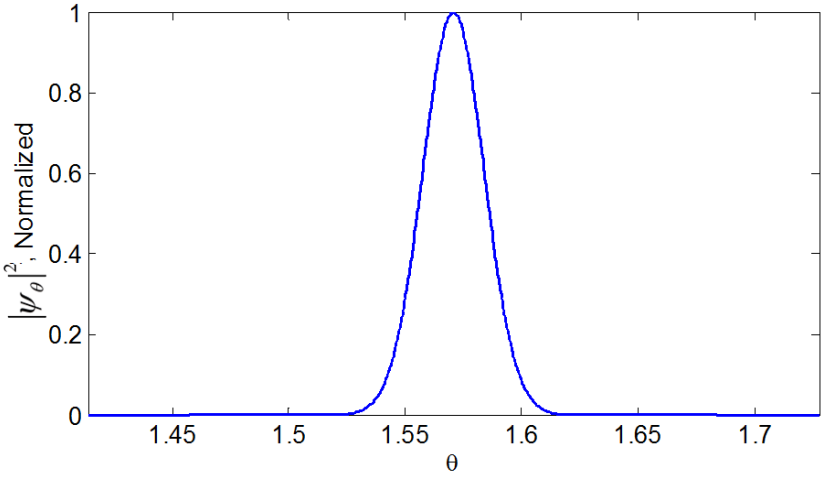

Figure 5.10. Polar dependence of droplet WGM electric field profile (l = m).

From Fig. 5.7 and 5.10, it is shown that most of WGM power is strongly confined in a ring shape at resonator interface and in the equator plane. Including the azimuthal variation of WGM, the electric field of fundamental WGM in the equator plane is shown in Fig. 5.11 in which the white line represents the droplet interface.

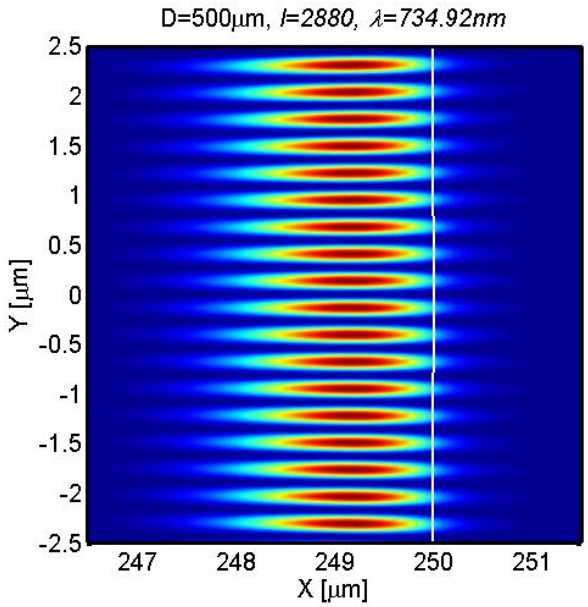

Figure 5.11. Magnified view of droplet WGM pattern in equator plane (white line represents the core-cladding interface).

5.3 WGM Transmission Measurement

As shown in Fig. 5.12, optical coupling into a droplet resonator is achieved using a tapered fiber placed proximate to the equator of droplet resonator. The laser source is a CW tunable laser (TLB-6711, New Focus, tunable range: $729-739nm$) and its wavelength is modulated by an external function generator that outputs triangular voltage from -2.5V to +2.5V. The optical transmission through a tapered fiber is measured by a 10 MHz photo-detector (PD) equipped with adjustable gain (2117-FC, New Focus). Transmitted optical power level is then recorded by a DAQ (USB-6211, National

Instruments) at a sampling frequency of 200 kHz where this becomes the limit of our system's measurement speed.

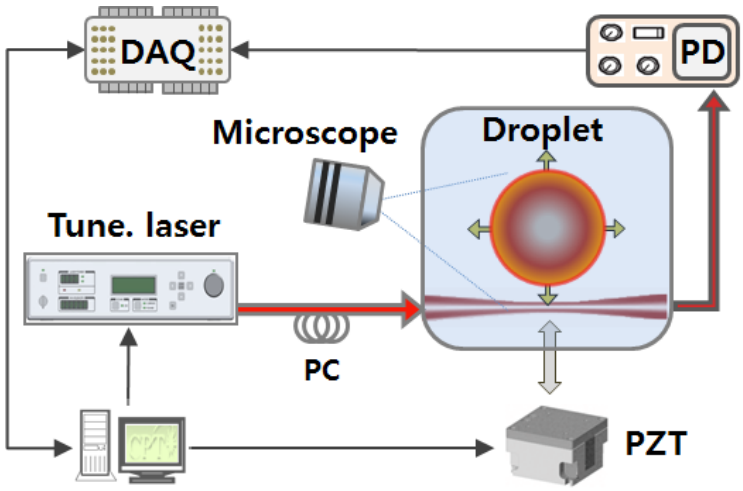

Figure 5.12. Schematic diagram of droplet WGM experiment setup.
The path of optical power is shown in red. (DAQ: data acquisition, PD: photo-detector, PC: polarization controller, PZT: piezo-electric transducer).

We use a nearly SM fiber (780HP, Thorlabs) to ensure that only the fundamental mode can be coupled into the resonator. Though such a non-single mode fiber at our laser wavelength may exhibit modal interferences, other types of SM fibers, (e.g. S630-HP, Thorlabs) with weaker mode confinement tend to experience very high transmission loss ($T < 5\%$) during taper fabrication process. Thus the 780HP model was the best choice in which the higher order mode is barely above its cut-off wavelength. A polarization controller is added in front of the taper for optimal coupling to either TE or TM polarized WGM. The coupling distance between tapered fiber and droplet resonator is tuned by a pizeo-stage (P611.3s, Physik Instrumente) with its positioning resolution of 1 nm. Two CCD cameras monitor the relative position of droplet and tapered fiber from side and top. In case there is a need of sample illumination for a clear view, a low-power dispersed

green laser beam is used. (Broadband light source is not preferred here due to the high absorbance in the water and possible temperature shift.)

All the electronic devices equipped with cooling fan are isolated from the optical table surface by inserting shock absorbers underneath the devices. Also the water chamber that contains the droplet resonator and tapered fiber is isolated from the air flow in the experimental condition by surrounding the entire chamber with custom-built chamber as shown in Fig. 5.13.

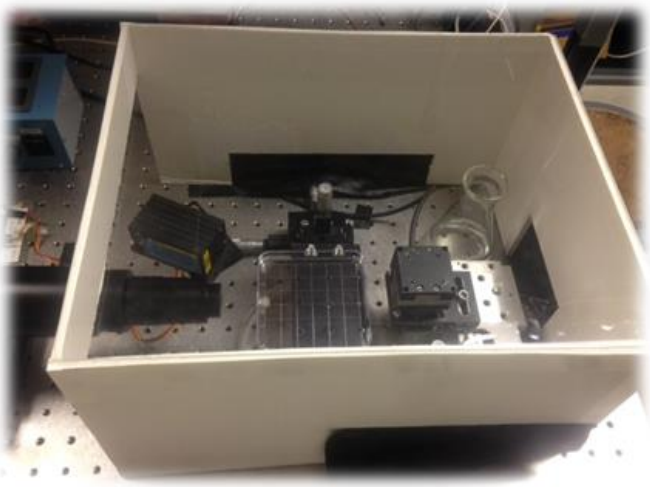

Figure 5.13. Top view of droplet WGM coupling setup enclosed in chamber.

References

1. J. C. Knight, G. Cheung, F. Jacques, and T. A. Birks, “Phase-matched excitation of whispering-gallery-mode resonances by a fiber taper,” *Opt. Lett*. Vol. 2 2, No. 15, pp. 1129–1131, 1997.

2. L. Ding, C. Belacel, S. Ducci, G. Leo, and I. Favero, “Ultralow loss single-mode silica tapers manufactured by a microheater,” *Appl. Opt.*, Vol. 49, No. 13, May 2 010.

Chapter 6

Radiation Pressure Induced Nonlinearity

6.1 Experimental Results

We use a standard experimental configuration described in Fig. 5.12 to measure the resonance shifts of droplet WGM under different input powers. Fig. 6.1 shows a typical transmission spectrum of the droplet WGM, which contains multiple sharp dips, each associated with a high-*Q* WGM. Experimentally, the free-spectral-range (FSR) of the droplet is found to be $\Delta\lambda_{FSR} = 258pm$, which closely matches the theoretical estimation given by Eq. (2.12) as $\Delta\lambda_{FSR} \simeq \lambda^2/(2\pi nR) = 253pm$.

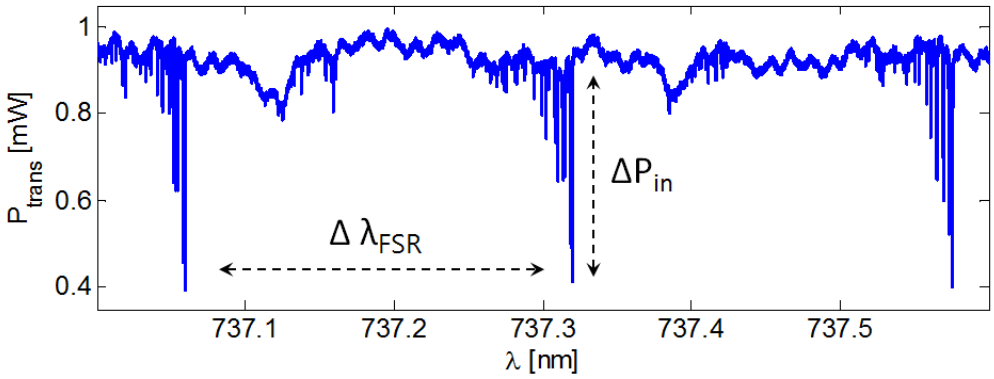

Figure 6.1. WGM transmission spectrum of a droplet resonator (D ~ 500 μm) with $\Delta\lambda_{FSR}$ = 258 pm and maximum coupling of ~60%.

For any given resonance dip, we use ΔP_{in} to denote the difference in transmitted optical powers between the on- and off-resoance case, as marked in Fig. 6.1. Given our droplet's relatively large size, we estimate that its *Q*-factor limited by radiation loss is very high ($Q_{rad} \sim 7\times10^8$) and can be safely ignored. Additionally, the interface of the

droplet is smooth at molecular level and should incur little scattering loss. Therefore, the *Q*-factor of our droplet resonator is mainly determined by the loss from taper-resonator coupling and material absorption. We can use the material absorption coefficient of the index matching fluid to estimate the absorption limited *Q* given by Eq. (2.3) as $Q_{abs} = 2\pi n / \alpha\lambda = 3.5\times10^7$. As to taper-resonator coupling, we can vary the coupling coefficient κ between the fiber taper and the droplet resonator by controlling the gap distance between the two using a piezo stage. As we adjust taper-resonator coupling, we also change the width of the WGM resonance and its *Q*-factor, the on-resonance transmission coefficent, and the value of ΔP_{in}. Experiementally, we operate in the under-coupled regime, with on-resonance transmission coefficient (T_{on}) in the range of 0.2 to 0.7. To accurately determine the *Q*-factor of the droplet resonator, we measure its transmission spectrum at low input power (8 μW), and find that *Q*-factor can vary in the range of 10^6 to 10^7. Since the resonator *Q*-factor is dominated by material absorption in the under-coupled regime, variations in its value can potentially be attributed to the presence of contaminants in core and cladding liquid.

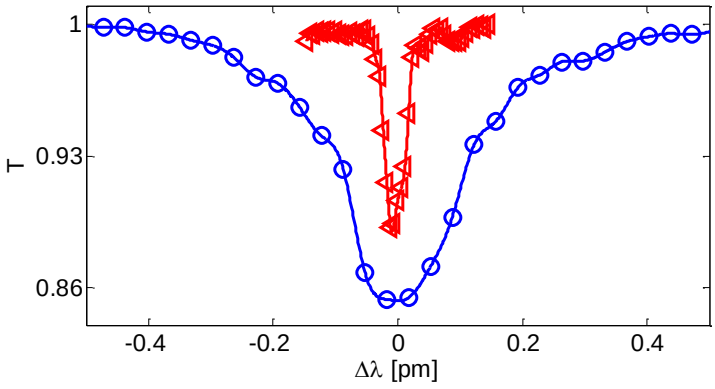

Figure 6.2. Examples of two droplet WGM resonances measured at low input power (cold resonances). (blue: low-*Q* ~2.1×10^6, red: high-*Q* ~1.7×10^7).

Figure. 6.2 shows two representative examples of the droplet transmission spectra measured at low input powers (cold resonances) (blue: lower $Q \sim 2.1\times10^6$, red: higher $Q \sim 1.7\times10^7$). We note that the higher Q is reasonably close to Q_{abs} estimated above, which is the theoretical upper limit.

The transmission spectra in Fig. 6.3 is obtained by scanning the wavelength of a tunable laser (TL) at reasonably slow speed (V_{scan} = 1.17 nm/s) and input power $\Delta P_{in} = 200\mu W$. Interstingly, we find that the shapes of WGM resonances generally depend on the direction of laser scan. Here, we use up-scan (or down-scan) to denote the cases where we increase (or decrease) the tunable laser wavelength. For up-scans (blue curve in Fig. 6.3), we find that the shapes of WGM resonances often resemble those of right triangles with a gentle downward slope followed by sharp recovery that are often reported in the researches of thermally induced nonlinearity [1-4]. We use $\Delta\lambda_{res}$ to represent the scale of red-shift in up-scan. In contrast, for down-scans, WGM resonances show much narrower linewidths, as can be seen as red curve in Fig. 6.3.

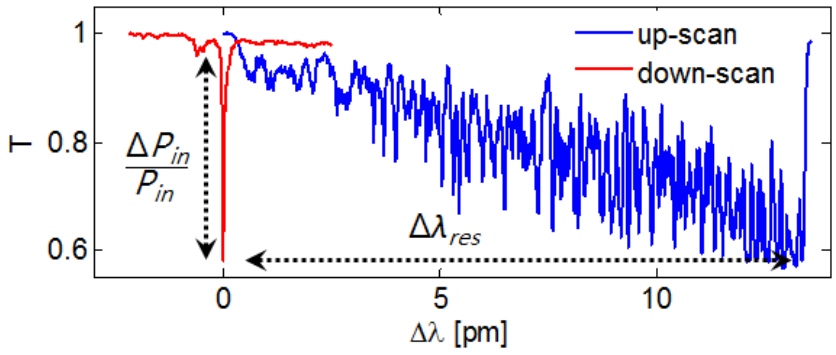

Figure 6.3. Deformed shapes of WGM resonance observed in up-scan (blue) and down-scan (red). The linewidth of red curve (down-scan) is found to be narrower than the cold resonance. (V_{scan} = 1.17 nm/s) ($\Delta P_{in} = 200\ \mu W$)

Qualitatively, the red-shifts of WGM resonances observed during up-scans can be explained as follows. As the tunable laser wavelength approaches a WGM resonance, the optical power carried by the WGM increases. The radiation pressure of the WGM can thus deform the droplet, push its interface outwards, and produce a red-shift in the resonance wavelength. During up-scans, with appropriate scanning speed, the tunable laser wavelength can potentially match the shift in WGM resonance and produce the transmission spectrum in Fig. 6.3 (blue). The noise in down-slope is originated from the thermal fluctuation of droplet interface [5-10]. For down-scans shown as red in Fig. 6.3, the shift in laser wavelength and the radiation-pressure induced resonance shift are opposite in direction. Therefore as soon as the laser wavelength comes into the red-side of cold resonance, the resonance shifts (jumps) to the red-side of laser wavelength and there will be only a sharp dip appears in the transmission spectrum.

6.1.1 Up-scan WGM Spectra

To experimentally confirm the linear relation between the input power (ΔP_{in}) and the scale of resonance shift ($\Delta\lambda_{res}$) during up-scan, we first record ~6000 different transmission spectra for an identical droplet resonator while varying ΔP_{in} from $20\mu W$ up to $200\mu W$. Then we use a specific resonance showing the highest coupling among others appearing in each WGM spectrum and extract the ΔP_{in} and $\Delta\lambda_{res}$ using a customized fitting method that will be described in chapter 6.2.2. Experimental results measured at different laser scan speeds ($V_{scan} = 1.17, 2.33, 3.50,$ and $7.00 nm/s$) are shown in Fig. 6.4(a)-(d), respectively. Red curves represent the HO model results done with following

parameters: $Q = 1.5 \times 10^6$, $\tau_r = \tau_c = 0.997$, $\mu = 15mPas$, $\sigma = 18mN/m$, and $P_{sat} = 2048W$. The same parameters are used for all the rest of analysis in this manuscript if not specified. Black dashed curves represent the linear estimation of resonance shift using Eq. (4.21) with an absorption coefficient ($\alpha = 3.8m^{-1}$) which is found from the given WGM loss factor parameter ($\tau_r = 0.997$) that is used in HO model. When the material absorption of a WGM resonator is assumed to be a dominant loss factor, the absorption coefficient and the WGM loss factor can be related as follows,

$$\alpha = -\ln(\tau_r)/(\pi R). \tag{6.1}$$

When choosing the simulation parameters, we first find the typical linewidth of cold resonances and estimate the *Q*-factor. Then we can find the τ_r and τ_c from the estimated *Q* based on our previous assumption that the *Q*-factor is limited by absorption loss. After all, the interfacial tension (σ) and viscosity (μ) of droplet become the only fitting parameters left. Finally, P_{sat} is not a free parameter: its value is determined by applying the steady-state analysis in section 4.1 with a given surface tension $\sigma = 18mN/m$. The values of σ and μ are also close to the material properties of index matching fluid, as specified in the product specification sheet.

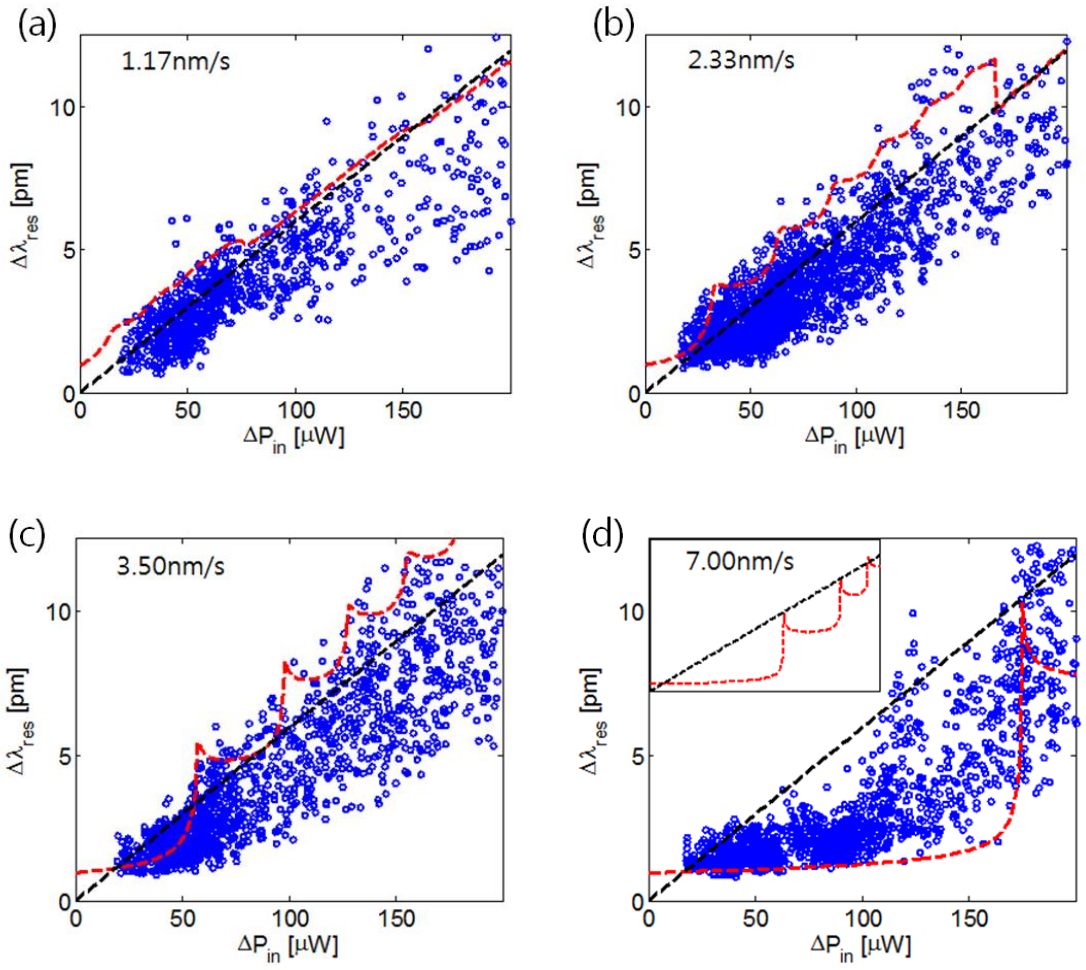

Figure 6.4. Experimental result of radiation pressure induced resonance shift (blue dots). Each figure comes from different V_{scan}: (a) 1.17nm/s, (b) 2.33nm/s, (c) 3.50nm/s, and (d) 7.00nm/s. (Black-dashed line: steady-state estimation, red-dashed curve: HO model)

In general, experimental results in Fig. 6.4(a)-(c) measured at V_{scan} = 1.17, 2.33, and 3.50 nm/s mostly follow the linear relation of $\Delta\lambda_{res} / \Delta P_{in} = 60\ fm \cdot \mu W^{-1}$, where the actual droplet deformation at input power of $200\mu W$ can be estimated to be $\Delta R = 4.1nm$. However, for a fast laser scan in Fig. 6.4(d) (V_{scan} = 7.00 nm/s), our result suggests that $\Delta\lambda_{res}$ remains relatively small for $\Delta P_{in} < 100\mu W$ and then rapidly increases once the ΔP_{in} exceeds $100\mu W$. (HO model also shows a similar threshold behavior. Simulation result for input powers of up to $300\mu W$ is also added as inset of Fig. 6.4(d) to show the

further trend.) The R-squared of linear regression in each result are 0.58, 0.59, 0.58, and -0.11, respectively. As described in earlier section, in case of reasonably slow laser scan, the laser wavelength matches the shift of WGM resonance and they smoothly drift together towards higher wavelength. In such a condition, the linear relation of $\Delta\lambda_{res}$ and ΔP_{in} holds. However, as the low R-squared of linear regression for the fast laser scan suggests (-0.11 at V_{scan} = 7.00 nm/s), there is different temporal dynamics of resonance shift process at fast laser scan.

The difference between slow and fast scans can also be seen from the measured transmission spectra. Fig. 6.5(a) shows a typical slow-scan WGM transmission spectrum (blue line) as well as the corresponding simulation (red dashed line), where we normalize the off-resonance transmission to be 1 and the on-resonance transmission to be 0. To facilitate comparison, we apply a low pass filter to minimize the impact of measurement noises. (A typical un-filtered transmission spectrum is shown in cyan dots.) For relatively slow scans, the laser wavelength can match the shift of WGM resonance (due to radiation pressure), and then they can smoothly "move" in tandem and shift towards longer wavelength. On the other hand, when the laser approaches the resonance at relatively fast speed (Fig. 6.5(b)), the small fraction of optical power coupled at blue-side (left) tail of resonance is not enough to generate fast resonance shift compared to the approaching speed of laser wavelength. Then the laser wavelength reaches far inside of resonance while the resonance position is still nearly stationary and the resulting sudden increase of WGM power shifts the resonance abruptly. For this reason, the transmission spectra at fast scan speed takes a form of repeating dips (kicking motion) as shown in Fig. 6.5(b) rather than the triangular shape shown in Fig. 6.5(a). The experimental result with no-

resonance shift at $V_{scan} = 7.00nm/s$ and $\Delta P_{in} < 100\mu W$ in Fig. 6.4.(d) is such a case that the coupled optical power was not sufficient to induce a resonance shift faster than the laser scan. Further increase of scan speed will require higher input power to generate observable resonance shift.

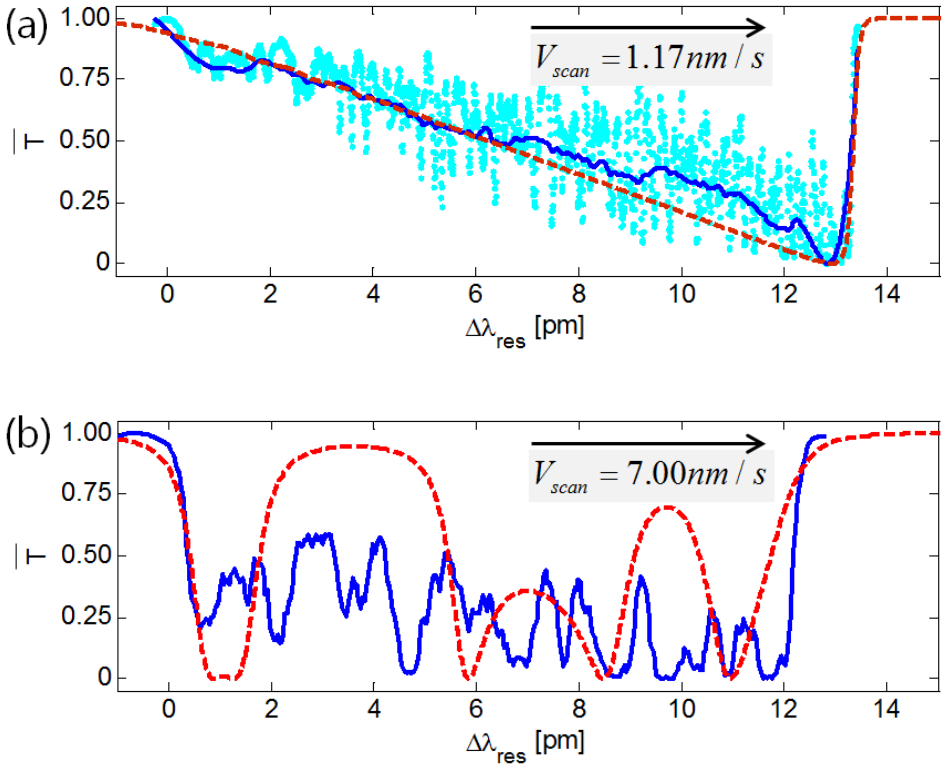

Figure 6.5. Different shapes of WGM resonance shift at different up-scan speeds. Blue curves represent the experimental observations and red dashed curves are obtained from HO model. (a) Slow-scan (V_{scan} = 1.17nm/s), (b) fast-scan (V_{scan} = 7.00nm/s).

We can estimate the impact of thermal noises in our measurements through following considerations. Imagine that the radius of a spherical droplet changes from R_0 to $R_0 + \Delta R$ at the equator. Assuming a spheroid shape for the deformed droplet, the increase in droplet's surface area (ΔS) can be approximated as,

$$\Delta S = S_{spheroid} - S_{sphere} \simeq 20 \cdot \Delta R^2 \qquad (6.2)$$

which should increase the surface energy of the droplet by $\Delta E_{surf.} = 20\sigma\Delta R^2$. We can equate this energy change to the thermal energy $E_{therm} = k_B T$, where $k_B = 1.38\times10^{-23} J/K$ is Boltzmann constant and T is temperature. Thus, the scale of thermally induced droplet surface fluctuation ΔR_{therm} can be estimated as

$$\Delta R_{therm} \simeq \sqrt{k_B T / 20\sigma} \tag{6.3}$$

Assuming $\sigma = 18 mN/m$ and $T = 300K$, we find that the thermal fluctuation ΔR_{therm} is roughly 1 Å. For our $\sim 250\mu m$ radius droplet, the corresponding thermally induced fluctuation of WGM resonance wavelength $\Delta\lambda_{res,therm}$ is approximately 0.3 pm. This simple calculation provides a correct order of magnitude estimate of the noise floor in our $\Delta\lambda_{res}$ measurements (results in Fig. 6.4).

Potentially, the radiation pressure induced resonance shift can be terminated due to thermal or environmental noises. For example, acoustic wave and mechanical vibration can deform the interface of droplet resonator and these can also be attributed to the deviation of experimental data in Fig. 6.4.

Typical *Q*-factor estimated from the linewidth of cold resonances at relatively low ΔP_{in} in Fig. 6.4 is found to be in a range of $1\times10^6 \sim 2\times10^6$. Varying absorption coefficient (due to contamination), multimode coupling with different *Q*-factors, and varying coupling coefficient can account for these deviations of *Q*.

Optical transmission along the taper submerged in the cladding liquid (water) slowly drops by time during the entire experiment due to contamination and water absorption. Therefore, it should be noted that the actual input power coupled into the

resonator can be 1~2 times higher than the experimentally observed power level at the output-side of taper.

6.1.2 Down-scan WGM Spectra

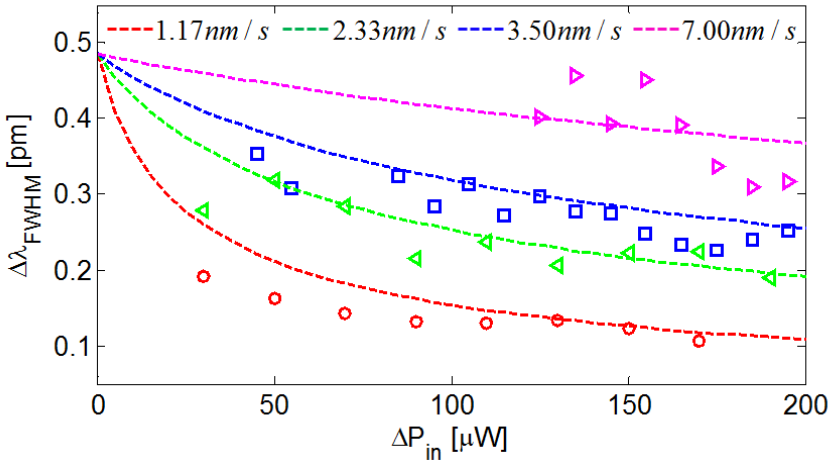

Figure 6.6. Linewidth of squeezed resonance shape in down-scan at different V_{scan} and ΔP_{in}. (Dots: experimental results, Dashed curves: HO simulation) (red: 1.17 nm/s, green: 2.33nm/s, blue: 3.50nm/s, magenta: 7.00nm/s).

In contrast with up-scan measurements, the WGM resonances obtained during down-scans retain their narrow linewidths. This is because laser wavelength is decreased during down scans, yet radiation pressure pushes the droplet outwards and shifts WGM resonances towards longer wavelengths. Therefore, the net result is a reduction of resonance linewidth measured in the WGM transmission spectrum. Fig. 6.6 shows the power dependence of the full width half maximum of WGM resonance ($\Delta\lambda_{FWHM}$) under four different laser scan speeds. Markers and dashed curves represent, respectively, experimentally measured linewidth and HO model result. Different colors are used to represent different V_{scan}. Each experimental data point is an average of 5 to 20 linewidth

measurements at the similar range of ΔP_{in}. This analysis is only meaningful in statistical manner due to the sharp linewidth comparable to the resolution limit of experiment system. We can also use the HO model to simulate the narrowing of WGM linewidths during down scans, where the parameters are the same as those in Fig. 6.4. In general, the reduction of linewidth is related to the speed of droplet deformation and more pronounced under a circumstance at the use of higher ΔP_{in} (stronger force acting on droplet surface) and slower V_{scan} (longer time for acceleration). As the droplet deforms faster, the resonance wavelength crosses over the laser wavelength in a shorter time and leaves narrower shape of resonance in WGM transmission spectrum.

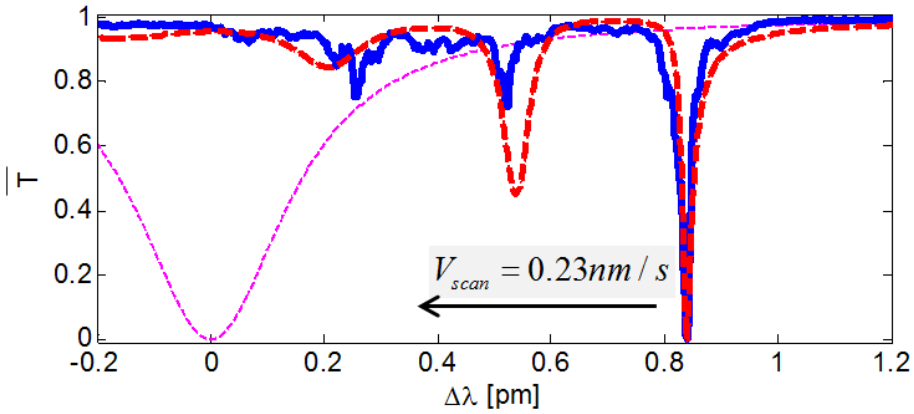

Figure 6.7. WGM transmission spectrum during down-scan.
(blue: experimental result, red: HO model, magenta: cold resonance).

In addition, an interesting feature of radiation pressure driven nonlinearity can be discussed with a WGM transmission spectrum measured during slow down-scan across a resonance shown in Fig. 6.7 (blue solid curve: experimental result, red dashed curve: HO model, magenta dashed curve: cold resonance) (HO model: $Q = 2.3\times10^6$, $\tau_r = \tau_c = 0.998$, $\Delta P_{in} = 100\mu W$, V_{scan} = 0.23 nm/s). The 3~4 dips appearing in the spectrum represent the multi-crossing of laser wavelength and a time-varying resonance

location modulated by the coupled optical power of WGM. As the laser wavelength approaches from the red-side tail of cold resonance, a fraction of WGM coupling and following radiation pressure shifts resonance toward higher wavelength, where it enables even stronger WGM coupling. Even for a short time after the laser wavelength passes the shifted on-resonance (major dip in spectrum), there is an additional increase in resonance wavelength due to the inertial motion of droplet surface. Such a process triggers a "slingshot" motion of droplet surface, where soon the shifted resonance recovers toward the cold resonance by the surface tension of droplet. In contrast to the first encounter, the second encounter (second dip in spectrum) is made by the chase of recovering resonance from the red-side of laser wavelength. The second encounter again red-shifts the resonance and the same process repeats until the laser wavelength completely passes original location of resonance. Such an observation of dynamic interplay between the surface energy of droplet and WGM induced radiation pressure is distinguishable from the others seen in relaxation type nonlinearities (e.g. thermally induced nonlinearity [11]).

6.2 HO Simulation Results

6.2.1 Resonance Shift at Different Parameters

As the experimental results in Fig. 6.5 shows, using different laser scan speed (V_{scan}) and optical power can significantly change the shape of WGM transmission spectra. Here we use our HO model described in chapter 4.2 to analyze radiation pressure induced droplet deformation with different viscosity (μ) and surface tension (σ) values. This allows us to compare the different shapes of WGM transmission spectra that can potentially be

observed in other droplet resonators made of different fluidic parameters. Figure 6.8 (a), (b), and (c) show the HO simulation results with different values of V_{scan}, μ, and σ, respectively. If not mentioned, the other simulation parameters are set to be as follow: $Q = 1.5\times10^6$, $\tau_r = \tau_c = 0.997$, $V_{scan} = 3nm/s$, $\mu = 15.3\,mPa\cdot s$, $\sigma = 18mN/m$, and $\Delta P_{in} = 200\mu W$.

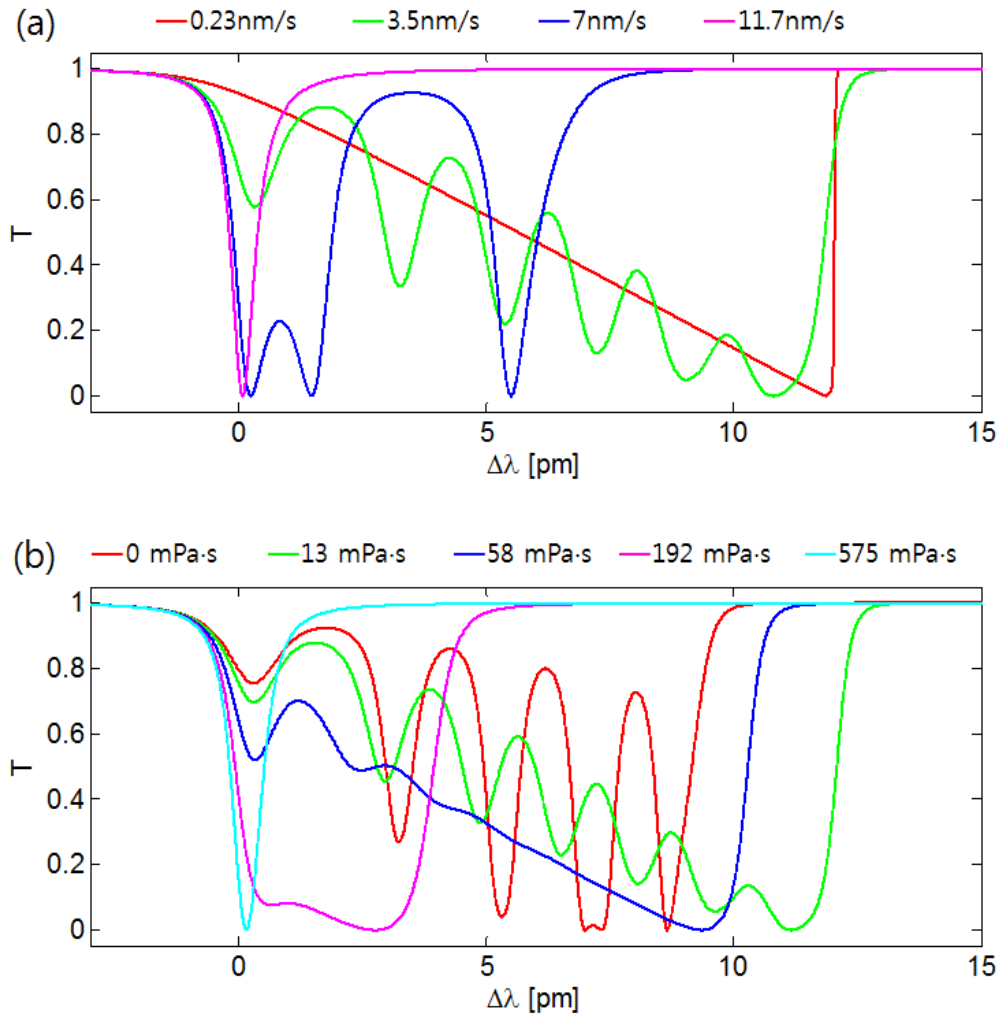

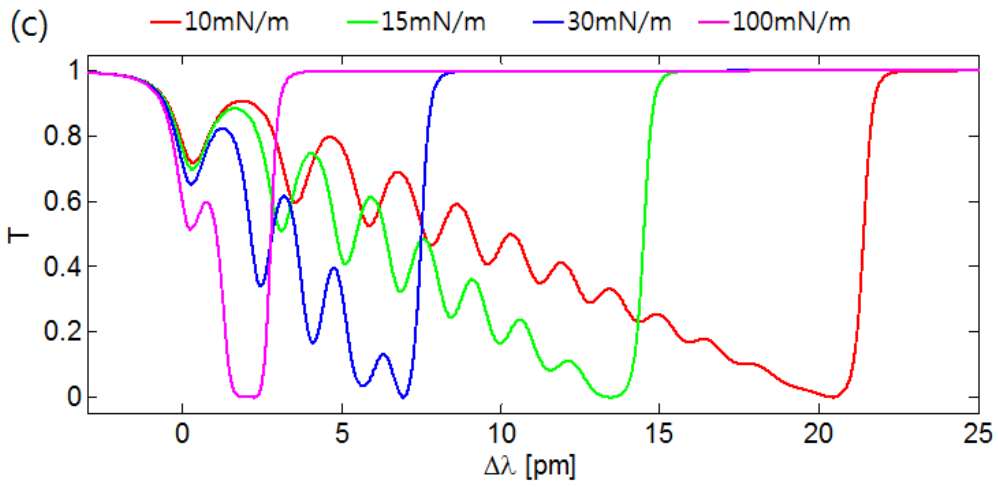

Figure 6.8. WGM transmission spectra simulated by HO model at different, (a) laser scan speeds, (b) viscosities, and (c) surface tensions.

In Fig. 6.8(a), as the laser scans faster, the amplitude of oscillation in transmission spectrum increases while the amount of resonance shift decreases. The results in Fig. 6.8(b) suggest that if the droplet is more viscous, the amplitude of oscillation of the transmission spectrum decreases. An interesting feature in Fig. 6.8(b) is that droplets with very high viscosity tend to produce smaller resonance shift. However, if we increase liquid viscosity from 0 to 13 $mPa \cdot s$, the more viscos droplet actually produces a greater resonance shift. Finally, in Fig. 6.8(c), we consider liquid droplets with different interfacial tension. Clearly, droplets with higher interfacial tension can significantly decrease the amount of resonance shift. This is to be expected, since higher surface tension increases the P_{sat}, as described in chapter 4.1. Finally, the frequency of oscillation increases due to the faster response of interfacial motion ($f = \sqrt{2\sigma / \pi^2 \rho R^3}$) at higher surface tension.

6.2.2 Algorithm of Resonance Shift Extraction

Unlike in simulations, where we can directly compare the original and the shifted WGM resonance, in experiments, it is not easy to directly measure the value of $\Delta\lambda_{res}$. Instead, we use the following method to extract $\Delta\lambda_{res}$. As an example, an experimentally observed red-shifted resonance is shown in Fig. 6.9 (blue solid curve), where we normalize the off-resonance transmission to be 1. We first determine two points (yellow circles) in the transmission spectrum, where the transmission coefficients at these two points equal $T = 0.75 + 0.25T_{on}$, which is equivalent to 75% of the resonance depth. Then, we calculate the average of the two yellow circles, and set the transmission at the average of the two wavelengths to be be $T = T_{on}$. Then we utilize a second order polynomial to fit the transmission coefficients at these three wavelengths (the red dashed line). Based on the polynomial, we can calculate two wavelengths (the green circles in the figure) at which the normalized transmission coefficient becomes 1. The difference between the two wavelengths is the estimated $\Delta\lambda_{res}$.

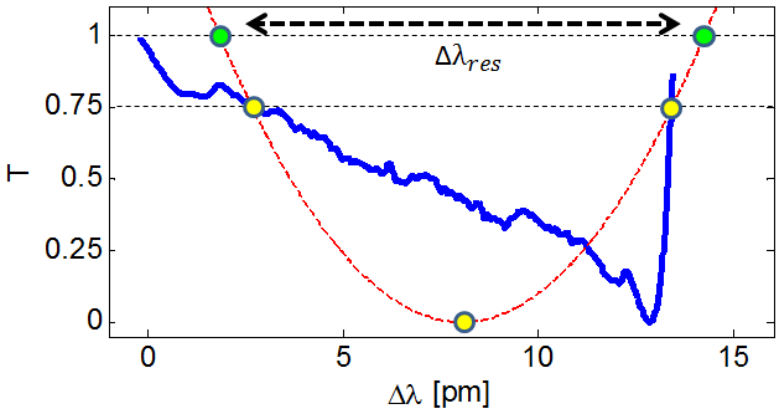

Figure 6.9. Algorithm of resonance shift estimation from experimentally observed deformed shape of resonance. (Blue: WGM transmission spectrum, Red: 2nd order polynomial fitting)

In HO simulations, we can use three different techniques to determine the magnitude of resonance shift:

1. The 2nd order polynomial fitting trace described above.
2. Find the wavelength at minimum transmission of red-shifted resonance and subtract it with the cold resonance wavelength.
3. Find the maximum deformation (ΔR) of droplet and convert it to the resonance shift using Eq. (4.13) and (4.15).

In principle, the third technique may show the best result matching to the definition of 'resonance shift'. However, we use the first method to ensure that experimentally measured and the simulated $\Delta\lambda_{res}$ are determined using the same method. Figure 6.10 compares the simulated values of $\Delta\lambda_{res}$ determined using the three different techniques described above (Fig. 6.10(a): $V_{scan} = 1.17 nm/s$)(Fig. 6.10(b): $7.00 nm/s$). The values of $\Delta\lambda_{res}$ determined through 2nd order polynomial fitting (the first method) and ΔR (the third method) closely track each other, where the differences between the two methods are within measurement errors. The second method, where we use the minimum transmission to determine $\Delta\lambda_{res}$, is less reliable, especially for fast scan results. This is to be expected, given the rapid oscillation of the transmission spectrum in Fig. 6.5(b). Based on the results in Fig. 6.10, we use the fitting-trace method for both experimental and simulation results.

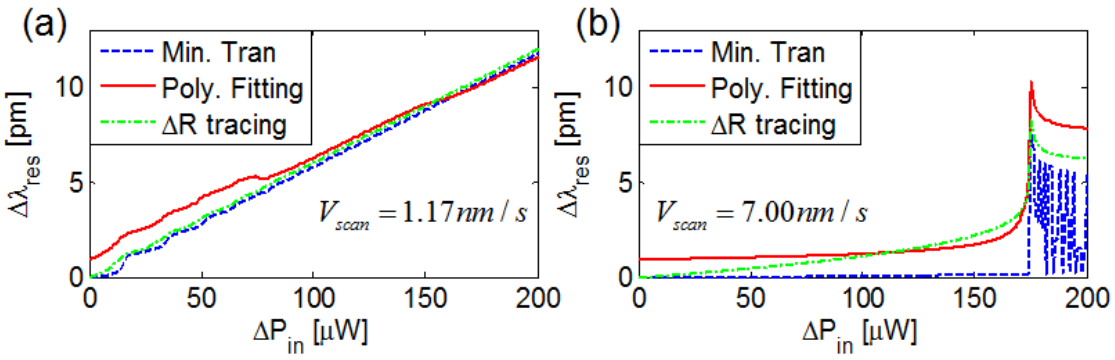

Figure 6.10. Comparison of data processing techniques used in the estimation of resonance shift in WGM transmission spectra.

6.2.3 The Impact of Under-coupling

For simplicity, in our HO model, we assume that the taper-resonator coupling satisfies the condition for critical coupling ($\tau_r = \tau_c$, $T_{on} = 0$). Experimentally, however, all observed WGM resonances are under-coupled and possess non-zero T_{on}. Based on Eq. (4.12), the maximum on-resonance WGM power satisfies

$$P_{WGM,on} = \frac{\tau_r^2}{1-\tau_r^2} \cdot (1-T_{on}) \cdot P_{in} = \frac{\tau_r^2}{1-\tau_r^2} \cdot \Delta P_{in} \tag{6.4}$$

where the right hand side of equation becomes independent of coupling coefficient (κ). To investigate the impact of under-coupling, we use the HO model to numerically calculate $\Delta\lambda_{res}$, where we vary the on resonance transmission (T_{on}) from 0 to ~1. To match experimental results, in our simulations, we adjust P_{in} such that the value of ΔP_{in} remains constant and equals to $200\mu W$. The results are shown in Fig. 6.11. At relatively slow laser scan speed (blue, $V_{scan} = 1\,nm/s$) the simulated value of $\Delta\lambda_{res}$ does not depend

significantly on the T_{on}. This supports our choice of assuming critical-coupling in our HO model simulations.

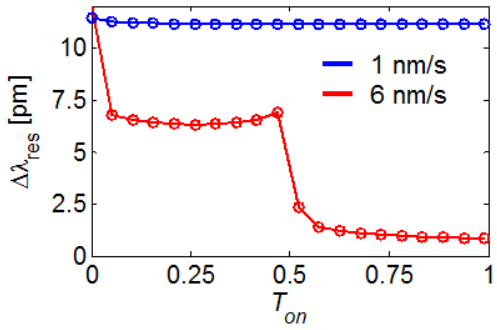

Figure 6.11. Resonance shift estimated by HO simulation for the resonances being excited using different coupling ratios while ΔP_{in} being constant.

When the laser scan speed becomes relatively fast (red, $V_{scan} = 6nm/s$), the T_{on} can impact the amount of resonance shift. This is because under-coupled WGMs tend to possess smaller linewidths, which in turn reduces the impact of radiation pressure on the droplet interface, even though the on-resonance WGM power ($P_{WGM,\,on}$) remains the same. This dependence on coupling conditions under fast scan may also explain the relatively large discrepancy between experimental results and HO predictions in Fig. 6.4(d).

References

1. I. Teraoka, “Analysis of thermal stabilization of whispering gallery mode resonan ce,” *Opt. Comm.*, Vol. 310, pp. 212-216, Aug. 2013.

2. C. Schmidt, A. Chipouline, T. Pertsch, A. Tünnermann, O. Egorov, F. Lederer, an d L. Deych, “Nonlinear thermal effects in optical microspheres at different wavel ength sweeping speeds,” *Opt. Express*, Vol. 16, No. 9, pp. 6286-6301, Apr. 2008.

3. C. Baker, S. Stapfner, D. Parrain, S. Ducci, G. Leo, E. M. Weig, and I. Favero, “Optical instability and self-pulsing in silicon nitride whispering gallery resonato r,” *Opt. Express*, Vol. 20, No. 27, pp. 29076-29089, 2012.

4. L. He, Y.-F. Xiao, J. Zhu, S. K. Ozdemir, and L. Yang, “Oscillatory thermal dyna mics in high-Q PDMS-coated silica toroidal microresonators,” *Opt. Express*, Vol. 17, No. 12, pp. 9571-9581, June 2009.

5. H. M. Lai, P. T. Leung, and K. Young, “Limitations on the photon storage lifetim e in electromagnetic resonances of highly transparent microdroplets,” *Phys. Rev. A*, Vol. 41, No. 9, pp. 5199-5204, May 1990.

6. A. Jonas, Y. Karadag, M. Mestre, and A. Kiraz, “Probing of ultrahigh optical Q-f actors of individual liquid microdroplets on superhydrophobic surfaces using tape red optical fiber waveguides,” *J. Opt. Soc. Am. B*, Vol. 29, No. 12, pp.3240, 2012.

7. B. M. Law, P. N. Segre, R. W. Gammon, and J. V. Sengers, “Light-scattering me asurements of entropy and viscous fluctuations in a liquid far from thermal equili brium,” *Phys. Rev. A*, Vol. 41, No. 2, pp. 816-824, Jan. 1990.

8. B. Davidovitch, E. Moro, and H. A. Stone, “Spreading of Viscous Fluid Drops on a Solid Substrate Assisted by Thermal Fluctuations,” *Phys. Rev. Lett.*, Vol. 95, N o. 24, Dec. 2005.

9. D. G. A. L. Aarts, M. Schmidt, and H. N. W. Lekkerkerker, “Direct Visual Obser vation of Thermal Capillary Waves,” *Science*, Vol. 304, pp. 847-850, May 2004.

10. V. V. Datsyuk, and I. A. Izmailov, “Optics of microdroplets,” *Phys.-Usp*, Vol. 44, No. 10, 2001.

11. T. Carmon, L. Yang, and K. J. Vahala, “Dynamical thermal behavior and thermal self-stability of microcavities,” *Opt. Express*, Vol. 12, No. 20, pp. 4742, 2004.

Chapter 7

Thermally Induced Nonlinearity

Recently, research on silica-based optical resonators has attracted much attention. Due to the extremely low material absorption and smooth surface, such resonators can support high quality (Q) factor whispering gallery modes (WGMs) in various geometries including microspheres [1], microtoroids [2], and cylinders [3, 4]. The existence of narrow WGM resonances can significantly enhance the optical power of the WGM, which can in turn enhance the efficiency of many nonlinear optical processes. Thermally induced nonlinearity has been reported by observing the shift of WGM resonances under different optical input powers [5-7]. Experimentally, it was found that under high optical input power, the resonance wavelength of a WGM in a solid resonator can shift towards longer wavelength. Such a nonlinear response is typically attributed to an increase in the temperature of the WGM resonator due to optical absorption. Most of the existing studies rely on WGM transmission measurement to indirectly infer the magnitude of temperature change. In this chapter, we present a method that can quantitatively evaluate the strength of thermal nonlinearity by using a FBG written within the fiber core to assess the temperature change of the WGM resonator.

In this study, we consider WGMs that circulate near the outer surface of a dielectric cylinder, which is simply a silica optical fiber with its polymer coating stripped off. In such cylindrical resonators, WGMs with Q factor in the range of 10^4 to 10^8 have been reported [4, 8, 9]. Experimentally, we use a fiber taper to excite WGMs that circulate near the surface of the silica fiber, with their propagation direction

perpendicular to the axial direction of cylinder. The spatial profiles of such WGMs can be determined using a modal analysis similar to the one we developed for WGMs in spherical resonators.

The experiments described here also allow us to estimate the impact of thermal nonlinearity in liquid droplet resonators. In two recent papers, we numerically evaluated the relative strength of several different types of nonlinear processes in droplet WGRs [10, 11]. Our results suggest that under a wide range of conditions, radiation pressure induced nonlinearity can be stronger than thermal nonlinearities such as thermo-optic effect, volume expansion, and thermos-capillary flow. It would be beneficial to supplement our theoretical analysis by experimentally assessing optical absorption induced temperature changes in high-*Q* optical resonators. For this purpose, we develop a new experimental method that can independently measure the temperature change of the optical resonator by directly writing a FBG within the fiber core of the cylindrical fiber. Then, we can use the peak wavelength of FBG reflection to determine the temperature shifts of the resonator.

7.1 Experiment Setup

7.1.1 FBG based Temperature Sensing

The temporal change of Bragg wavelength of FBG can be characterized by using either the transmission or reflection spectrum of the grating. A typical setup for measuring FBG transmission spectrum is shown in Fig. 7.1(a), where both the input and output ports of a standard FBG (custom fabricated by Ascentta Inc.) are spliced to a SMF (SMF-28, Corning) and connected to an optical spectrum analyzer (OSA, si720, Micron Optics),

which contains an internal sweeping laser source (5Hz) and a photo-detector. The wavelength resolution ($2.5pm$) and the laser linewidth ($4pm$) of OSA are much narrower than the linewidth of the FBG reflection peak.

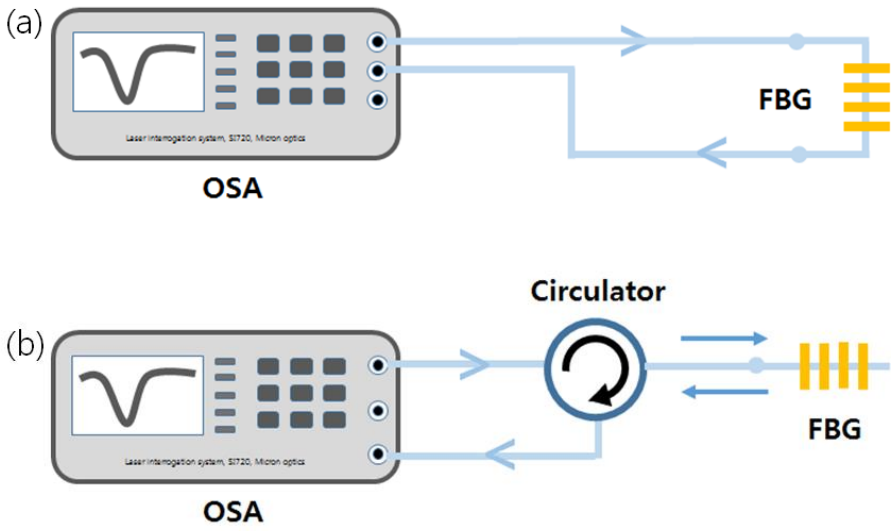

Figure 7.1. Schematic diagram of FBG spectrum measurement setup.
(a) Transmission signal measurement, (b) Reflection signal measurement.

The FBG reflection measurements can be carried out using almost the same setup, as shown in Fig. 7.1(b), where we introduce a circulator to separate the reflected signal from FBG and couple it back to the OSA. In our application, both the transmission and reflection measurement show similar sensing performance. However, for cases where space is limited, the reflection measurement can become preferable.

The performance of our FBG sensor is tested at room temperature. A typical transmission / reflection spectrum is shown in Fig. 7.2. The linewidth of FBG reflection is ~220 pm and the thermal coefficient of FBG reflection peak is $\alpha_{FBG} = 10pm/^{o}C$. With an appropriate data processing by using interpolation and Gaussian curve fitting, our FBG sample can detect a temperature change in the fiber at 0.02^{o}C level.

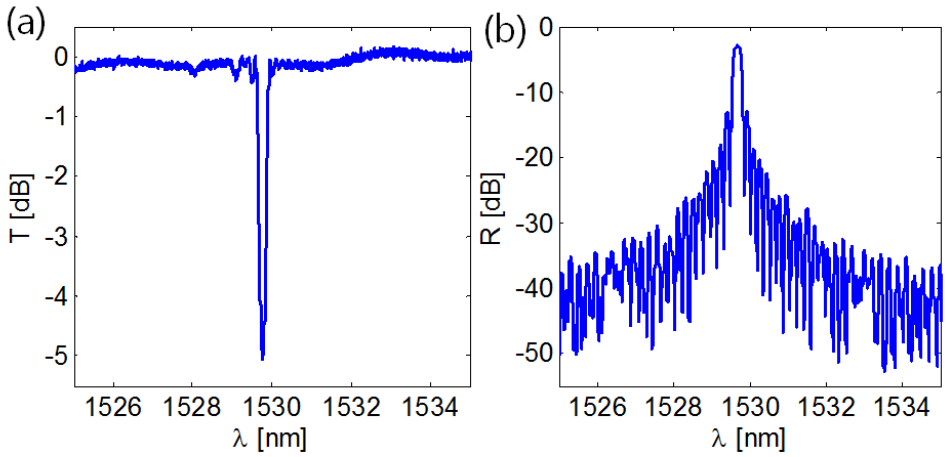

Figure 7.2. Representative spectra of FBG (a) transmission and (b) reflection.

The temporal stability of FBG is tested by placing the FBG in a sealed chamber and continuously measuring its peak reflection wavelength with 5 Hz sampling rate. The results are shown in Fig. 7.3 as blue curve, which possesses a standard deviation of ~ 0.44 pm. By taking the average of five adjacent data points, we can further reduce the standard deviation to ~ 0.20 pm (red curve in Fig. 7.3). Using the thermal coefficient of FBG $\alpha_{FBG} = 10\,pm/^{o}C$, the ultimate temperature resolution of our FBG sensor is $0.02^{o}C$.

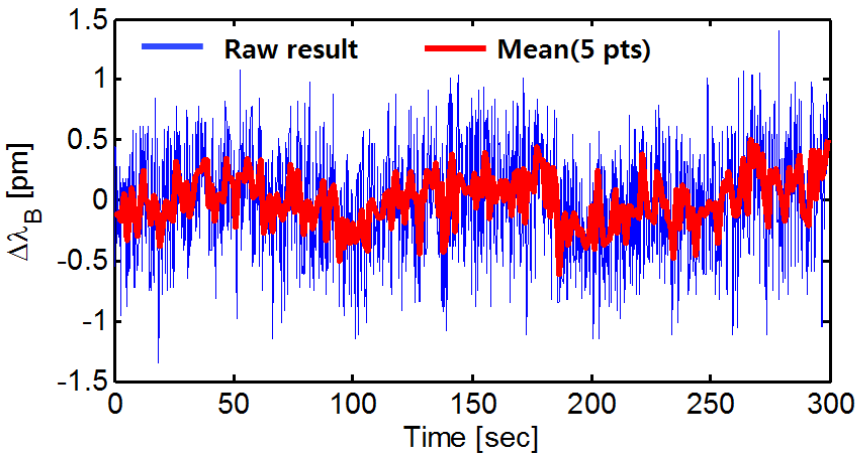

Figure 7.3. Temporal stability of FBG response tested in an air-sealed chamber. (Blue: raw data, Red: average over each of 5 data points).

7.1.2 WGM Coupling to Optical Fiber Resonator

Coupling light into a cylindrical resonator is much simpler than coupling light into a liquid droplet. Therefore, the experiment setup becomes quite simple. As shown in Fig. 7.4, there is no longer any need for taper alignment. Components such as piezo-stage and those for vibration control are no longer needed. Also, the length of the FBG is ~1 cm. Therefore, positioning the taper within the FBG can be easily achieved manually using a micrometer. The same tunable laser and photo-detector are used as other works in previous chapters.

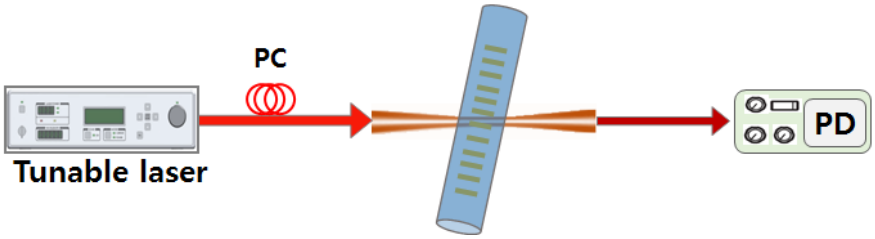

Figure 7.4. Schematic diagram of fiber WGM excitation setup.

A CCD camera image of coupled taper-resonator system is shown in Fig. 7.5(a). Due to the small diameter of tapered fiber ($D_{taper} = 500nm$) and the limited resolution of the camera, the shape of the taper cannot be clearly resolved in the image and is indicated using two yellow markers. As discussed in [3, 12, 13], due to the lack of axial confinement, the cylindrical resonator supports a continuum of WGMs, as described in Fig. 7.5(b).

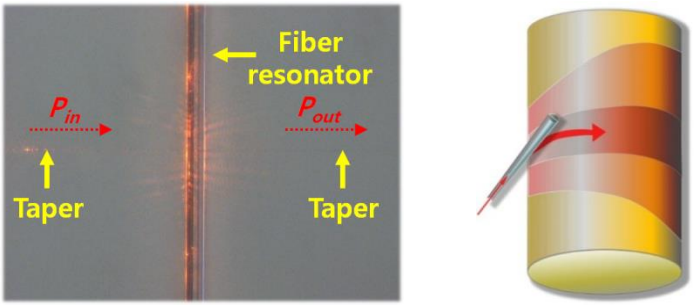

Figure 7.5. (a) Top view of taper-resonator coupling configuration taken by a CCD camera. (b) Schematic drawing of WGM paths in a cylindrical resonator.

The red glowing pattern along the length of fiber resonator shown in Fig. 7.5(a) can potentially be attributed to the so called 'spiral modes [13]'. Additionally, as the wavelength of the scanning laser approaches the WGM resonance, the glowing pattern tends to become stronger.

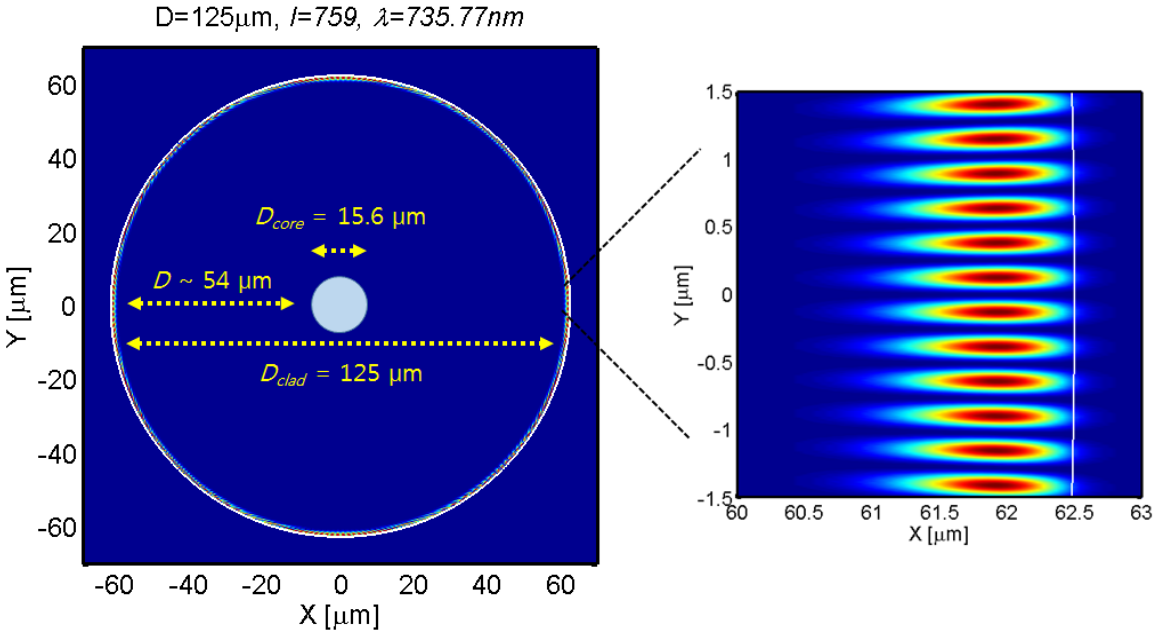

Figure 7.6. Cross sectional dimension of FBG based fiber resonator and WGM mode pattern (l = 758, λ = 735.55 nm, D = 125μm, in air).

As described in previous chapters, the radial dependence of WGM in a micro-resonator is tightly confined near the resonator surface. Fig. 7.6 shows the WGM field

distribution ($l = 758$, $\lambda = 735.55nm$, $D = 125\mu m$, in air) over the fiber cross-section. (Due to the small mode volume of WGM, a zoom-in view is added to the right.) There is a 50~60 μm gap between the WGM mode and the fiber core. Thus the temperature shift measured by the FBG might be different from that in the WGM region.

The radial dependences of fiber WGM in air and water are also shown in Fig. 7.7. Note that the y-axis of Fig. 7.7 is normalized such that the maximum field intensity becomes 1. There is a slight difference in the modal shapes but the distance between the core of the fiber and WGM mode remains almost same. Therefore, if a distinct difference in the thermal responses of the two controlled cases is detected, it can be mostly attributed to the different heat diffusivities of air and water.

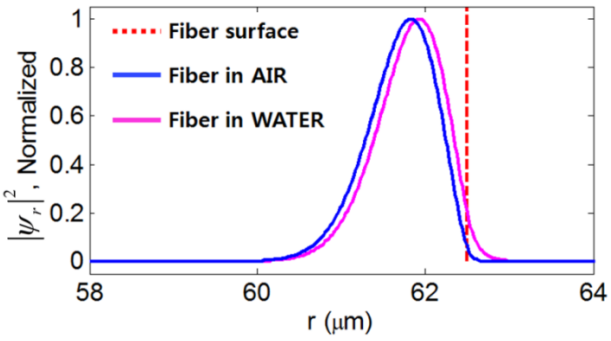

Figure 7.7. Radial dependence of fiber WGM in air (blue) and water (magenta) media.

Two examples of WGM transmission spectra of a fiber resonator are shown in Fig 7.8 where one on top (blue) is measured in air medium and the bottom one (red) is measured in water. From the given diameter of optical fiber ($D = 125\mu m$) and refractive index ($n = 1.45$), the free-spectral-range (FSR) of a fiber resonator is given as $FSR = 0.95nm$ by Eq. (2.12). From the experimentally observed spectra in Fig. 7.8, the FSRs in air and water media are shown to be 0.97 nm and 0.94 nm, respectively, and they closely match the theoretical predictions.

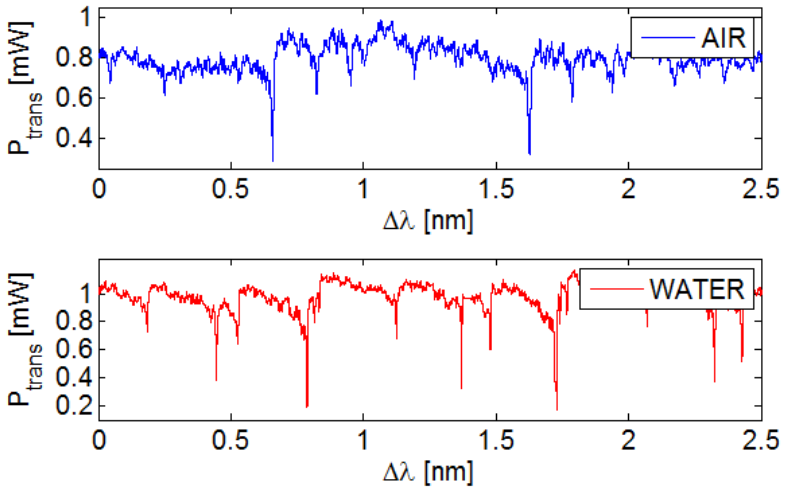

Figure 7.8. WGM transmission spectra of a fiber resonator measured in air (blue, top) and water (red, bottom) media.

Since water lowers the index contrast between core and cladding, the penetration depths of fiber WGM and tapered fiber are both enhanced. As a result, coupling into higher order modes, which correspond to the shallower dips in Fig. 7.8(b), becomes more likely. It should be noted that the resonance linewidth of fiber WGM can merely be used for a rough estimation of *Q*-factors due to the asymmetric shape of resonance as shown in Fig. 7.8 where each resonance dip has tails toward the shorter wavelength. Such resonance shapes are one of unique characteristics of cylindrical WGM resonators and these features make cylindrical resonators fundamentally different from other types of high-*Q* resonators (e.g., microsphere or microtoroids). In both the air and water media, *Q* of fundamental modes observed in our test are found to be in a range of $1\times10^5 \sim 2\times10^5$ whereas the higher order modes appearing in water medium case show relatively higher *Q* of up to 8×10^5. These *Q*-factors are assumed to be limited by the material absorption of fused silica at $\lambda = 735nm$.

7.2 WGM Induced Thermal Nonlinearity

In this chapter, we experimentally compare the strength of thermal nonlinearity in a fiber WGM resonator immersed in air and water. The thermal conductivity of air ($k_{air} = 0.026\,W/m\cdot K$) is more than an order of magnitude smaller than that of water ($k_{water} = 0.6\,W/m\cdot K$), which will lead to significantly different thermal behaviors. The power of WGM propagating in non-ideal material can be absorbed by resonator material and the equivalent amount of energy can be converted to thermal energy which increases the temperature of resonator volume and induces thermal nonlinearity. Thus the WGM can be assumed as a ring-shaped heat source around the circumference of resonator and its power is given by [14],

$$P_{heat} = 2\pi\alpha_{eff} a P_{WGM} \tag{7.1}$$

where α_{eff} is an effective absorption coefficient. As shown in the radial dependence of fiber WGM (Fig. 7.7), a fraction of optical power extends to environmental medium. For this case, the WGM not only experiences the material absorption of resonator, but also the one of surrounding medium can attribute to the absorption mechanism. Therefore we use the effective absorption coefficient that is given by [15],

$$\alpha_{eff} = \frac{P_{core}\cdot\alpha_{core} + P_{clad}\cdot\alpha_{clad}}{P_{core} + P_{clad}} = F_{core}\cdot\alpha_{core} + F_{clad}\cdot\alpha_{clad} \tag{7.2}$$

where F_{core} (F_{clad}) represents the ratio of WGM power in core (cladding) and total WGM power. At $\lambda = 735\,nm$, the absorption coefficients of typical fused silica [16] and water [17] are known to be ~ 2 m^{-1} and air is assumed to be transparent. As can be calculated by the radial dependence of WGM in Fig. 7.7, the parameters of WGM power ratios of air

medium and water medium cases are given as follows: $F_{core,air} = 290/291$, $F_{clad,air} = 1/291$, $F_{core,water} = 42/43$, and $F_{clad,water} = 1/43$. As a result, the effective absorption coefficients for both cases are determined to be ~ 2 m^{-1}. Given that most of WGM power is strongly confined inside the resonator surface, there is no surprise that the material absorption of core material governs the entire absorption loss of WGM.

In a high-*Q* WGM resonator with its *Q*-factor limited by material absorption, Eq. 7.1 can be approximated as

$$P_{heat} \simeq \tau_r \Delta P_{in} \tag{7.3}$$

where most of optical power coupled into the resonator will be converted to the thermal energy (for high-*Q*, $\tau_r \simeq 1$). Therefore as long as the same level of input power (ΔP_{in}) is used for WGM coupling, we can assume that no matter with cladding medium, the power of WGM heat source in our FBG based fiber will remain the same. Now it is proven that the two thermal nonlinearities (in air and water media) induced in our resonator sample can be tested in almost identical conditions except that the difference in thermal diffusivity (or conductivity) of air and water media remains as the only variable.

In experiment, we use the WGM coupling setup to couple light into the WGM circulating near the fiber resonator surface. Simultaneously, we measure the FBG reflection peak using the setup in Fig. 7.1(b). Meanwhile, FBG within the fiber core records the temperature-induced shift of Bragg wavelength ($\Delta\lambda_B$). We use different laser scan speeds (V_{scan}) to investigate the time dependence of thermally induced nonlinear responses. The fiber resonator is first tested in air. The results of WGM transmission spectra and $\Delta\lambda_B$ are shown in Fig. 7.9(a) and (b), respectively.

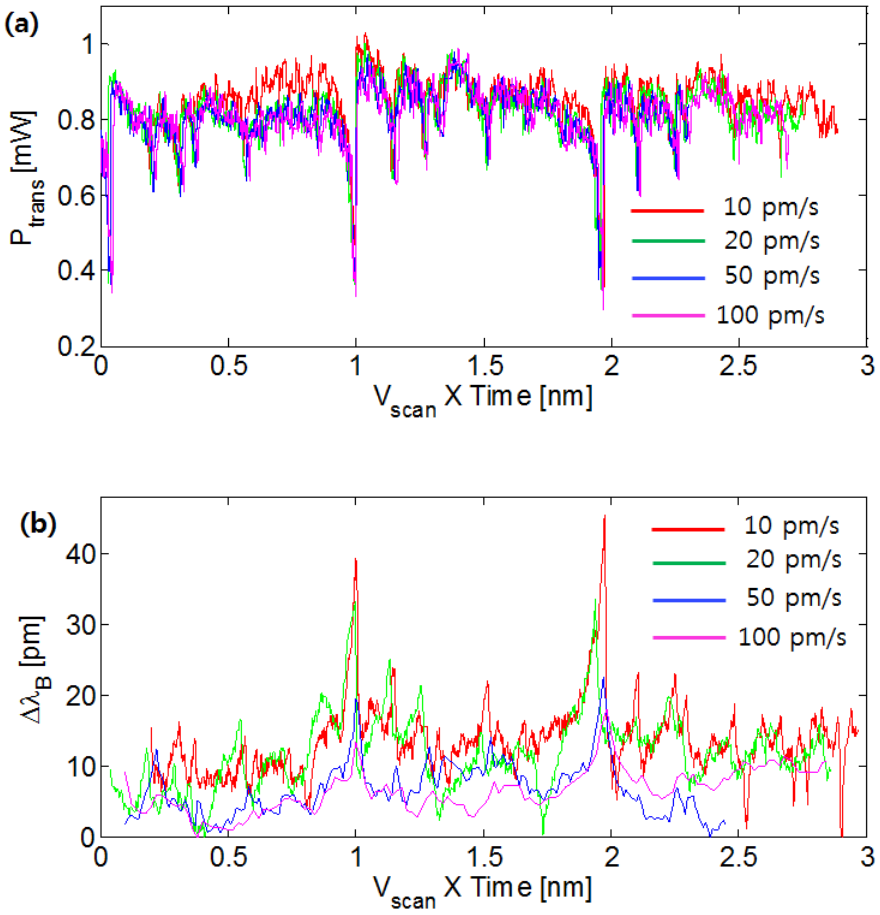

Figure 7.9. (a) Fiber WGM transmission spectra observed in air medium. (b) Bragg wavelength shift measured by FBG.

The result in Fig. 7.9 confirms that the excitation of the WGMs and the increase in fiber temperature are closely correlated. For example, at $V_{scan} = 10\,pm/s$, whenever a WGM is excited in the resonator ($\Delta P_{in} = 0.7mW$), a sharp temperature shift ($\Delta T = 4.5^{o}C$) is immediately detected by the FBG as well. A magnified view of Fig. 7.9(a) is given in Fig. 7.10 as grey curves to compare the thermally deformed shapes of a specific resonance at different V_{scan}. Due to the multiple mode appearance in the spectrum, numerical comparison of thermally-induced resonance shift cannot be made. However qualitatively speaking, the shape of resonance does not significantly change by the V_{scan} and an

average of the four curves is shown as a red dashed curve in Fig. 7.10 which represents a 'hot-resonance'. Here we confirm that the time scale of thermal nonlinearity at WGM mode volume [5] is shorter than the time given for a laser wavelength passing through a resonance ($50 \sim 500ms$ depends on laser scan speed). Besides, there is a blue dashed curve added which is recorded at a very fast V_{scan} to minimize the thermal nonlinearity and thus represents a 'cold-resonance'.

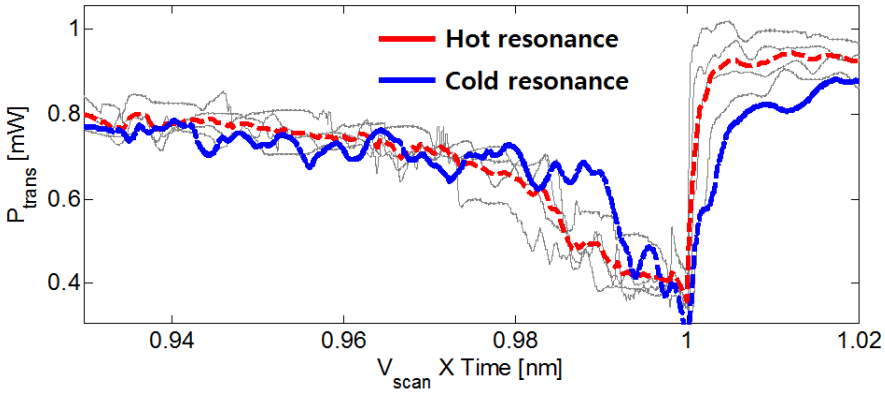

Figure 7.10. Comparison of thermally broaden WGM resonance (red dashed curve) and a cold resonance (blue dashed curve) observed in air medium.

In Fig. 7.10, hot resonance shows a few picometers of resonance drift toward the higher wavelength. The thermally shifted WGM resonance is given by [5],

$$\Delta\lambda_{res} \simeq \lambda \cdot \left[\varepsilon + \frac{1}{n}\frac{\partial n}{\partial T} \right] \cdot \Delta T = \lambda \cdot a_{therm} \cdot \Delta T \qquad (7.4)$$

where ε is expansion coefficient in $m/m^{o}C$. For fused silica, the thermal coefficient is known to be $\alpha_{therm} \sim 6\times10^{-6}\ \ ^{o}C^{-1}$ [18] and finally we have a simple relation between the resonance shift and temperature shift (ΔT) at our laser wavelength $\lambda = 735nm$ as,

$$\Delta\lambda_{res} \simeq 4.4 \cdot \Delta T\,[pm \cdot {}^{o}C^{-1} \cdot {}^{o}C]. \qquad (7.5)$$

Assuming the resonance shift (estimated by the difference between hot- and cold-resonances) shown in Fig. 7.10 is 10 pm at most, the temperature shift in WGM mode volume can be estimated to be $\sim 2.3^{o}C$.

Contrary to the estimation of temperature shift in the WGM mode volume which is found to be independent of V_{scan}, the Bragg wavelength shift ($\Delta\lambda_B$) measured by FBG in the center of fiber shows strong dependence on V_{scan} as shown in Fig. 7.11. (Each data point is an average of two repeated experimental results at identical condition.) Therefore, it can be assumed that the time scale of thermal energy diffusion from the WGM mode volume (mostly concentrated at resonator surface) into the core of fiber resonator is similar to the time scale of laser wavelength scan through a linewidth of a resonance ($50 \sim 500ms$). The thermal diffusion length is $\sim 54\mu m$ through a volume of fused silica as illustrated in Fig. 7.6.

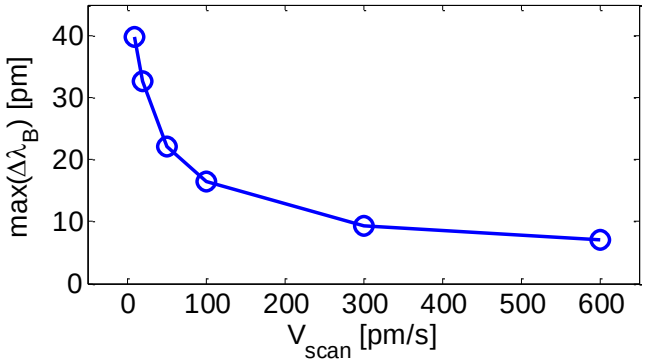

Figure 7.11. Maximum Bragg wavelength shift observed at different laser scan speeds.

The time scale of thermal energy diffusion throughout the volume of our resonator sample can also be estimated by the trend of thermal energy relaxation measured by the FBG. Figure 7.12 shows a pair of WGM transmission and the shift of Bragg wavelength measured at a time when the thermally induced resonance drift has

reached its maximum potential with given WGM power. At this moment, as soon as the laser wavelength escapes from the resonance ($t = 0$, marked as red vertical dashed line), the resonance quickly returns to its cold-resonance position and there is no more of thermal energy (originated from the absorption of WGM power) being supplied to the resonator volume. Therefore from $t = 0$, the temperature of FBG decays by time as shown in Fig. 7.12 as green curve and we find that the time scale of thermal energy relaxation (τ_{relax}) to be ~420 ms.

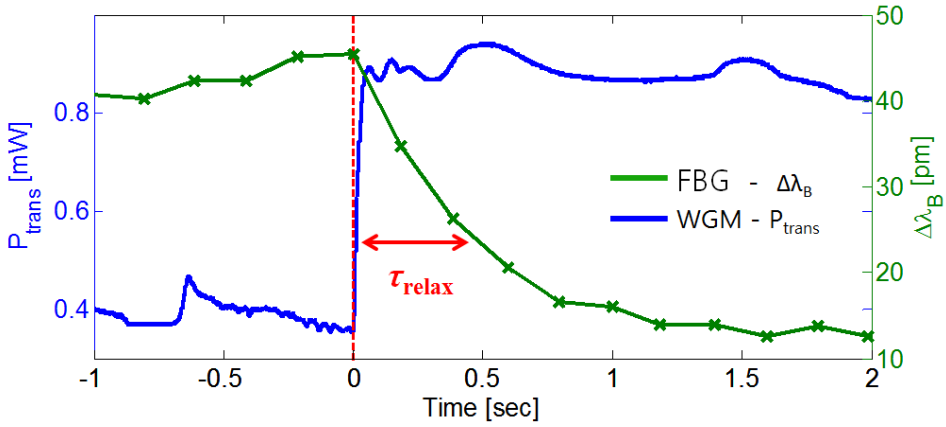

Figure 7.12. Time scale of thermal relaxation in a fiber core (FBG) at a moment of WGM power cut-off.

We can also refer to a previously reported thermal analysis (lumped capacity analysis) derived for silica micro-sphere given by [19] and use it as a rough estimation of thermal response time of our fiber resonator sample. The analysis assumes that there is a flow of heat energy between the microsphere and surrounding air medium due to their temperature difference. The analysis also assumes the temperature in the volume of microsphere is uniform. The time constant of the temperature response can be approximated as

$$\tau \sim \frac{2 \cdot \rho_{sphere} \cdot c_{sphere} \cdot r^2}{3 \cdot Nu \cdot k_{medium}} \tag{7.6}$$

where ρ_{sphere}, c_{sphere}, and r are the density, specific heat, and radius of the microsphere, respectively. Nu is a unit-less Nusselt number [20] and approximately ~2.1 for a microsphere in room temperature. For a microsphere ($\rho_{sphere} = 2.2 \times 10^3 kg/m^3$, $c_{sphere} = 703 J/kg \cdot K$, $r = 62.5 \mu m$) in air ($k_{air} = 0.026 W/m \cdot K$), the time constant is found to be $\sim 74\, ms$. The time constant measured in our experiment (~420 ms) is 6 times longer than the estimation given by Eq. (7.6), however, they are still in the same order of magnitude in spite of the rough assumptions.

Among all the Bragg wavelength shifts shown in Fig. 7.9(b), the longest shift is found to be $\Delta\lambda_B = 45.44 pm$ which measured at slowest V_{scan}. Therefore using the thermal coefficient of FBG ($\alpha_{FBG} = 10 pm/^oC$), the maximum ΔT at the center of fiber resonator is found to be $\sim 4.54\, ^oC$ which is even greater than the temperature shift in the heat source, i.e. WGM mode volume, ($\sim 2.3^oC$). In addition as can be predicted by Fig. 7.11, the temperature shift in the fiber core can be even higher if a TL with a further slow V_{scan} is used. Given that the higher scale of ΔT observed in fiber core than the fiber surface, we can confirm that the surrounding air medium is not functioning as a desirable heat sink.

There is one interesting feature of WGM in cylindrical resonator that can be seen in Fig. 7.9(b). The floor level of $\Delta\lambda_B$ measured by time fluctuates in a scale of ~10 pm even when there seems no sharp resonance appears. Given with the noise floor of FBG shown in Fig. 7.3 with a STD of 0.46pm ($\Delta T \simeq \Delta\lambda_B \times 0.1^oC/pm = 0.046^oC$), the

intrinsic noise of system cannot account for the excessive level of instability shown in Fig. 7.9(b). Here we use our previous analogy that the cylindrical resonators exhibit a continuum of WGMs along its axis. In this scenario, the effect of all weakly coupled continuums of spiral modes will appear in a WGM spectrum as a drop of signal level spanning over the entire wavelength range rather than showing up as a sharp dips at discrete wavelengths. Therefore, we can assume that the off-resonance temperature fluctuation in Fig. 7.9(b) is due to the heating of all spiral side WGMs. (Unlike the conventional terminology, the term 'off-resonance' is used to represent a moment when there is no appearance of high-*Q* WGM strongly confined on the normal cross sectional plane of resonator.) In other words, there will be a fraction of low-*Q* spiral WGMs coupled in the fiber resonator at all wavelengths.

In addition to the first test which is done for a fiber resonator in air medium, now we submerge the identical resonator sample in the water and repeat the same experimental procedures. Again as mentioned earlier, it should be noted that most of experimental parameters are well controlled within a factor of 2 for the two different media cases and the difference in thermal conductivities of air and water will play a key role to change the thermal responses of our fiber resonator sample. The test result from the measurement in water medium is shown in Fig. 7.13. Figure 7.13(b) shows that there is almost no temperature change in the core of fiber detected by the FBG at this time which is contrary to the previous air medium test.

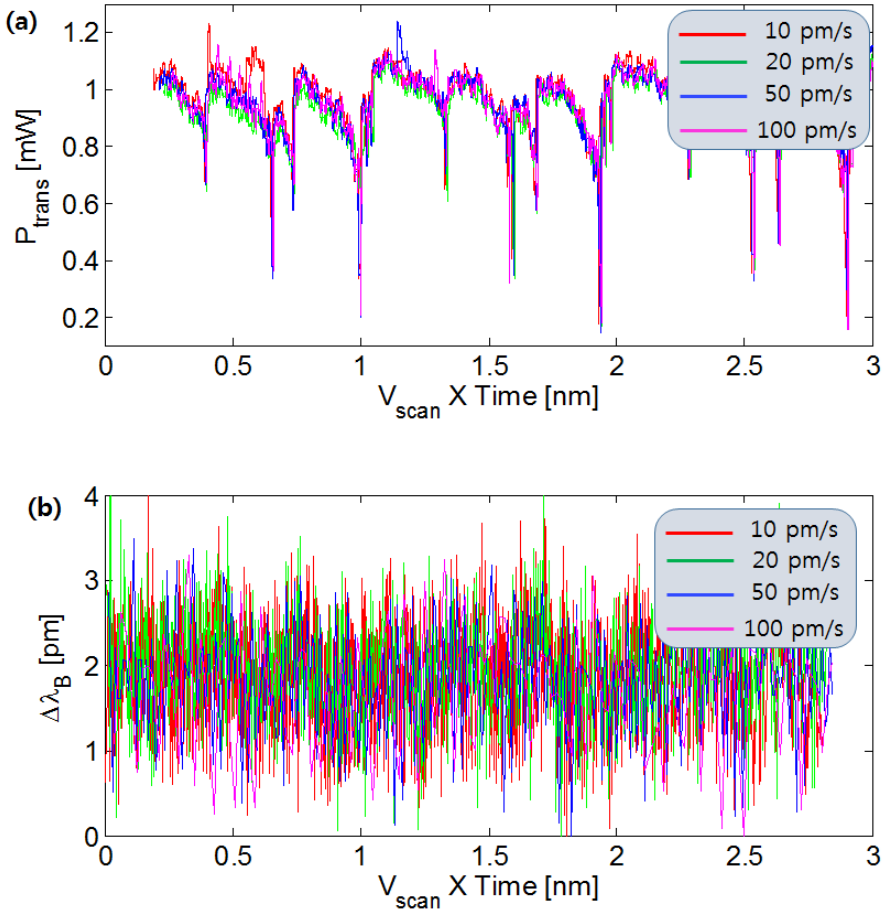

Figure 7.13. (a) Fiber WGM transmission spectra observed in water medium. (b) Bragg wavelength shift measured by FBG.

Similar to the analysis done in Fig. 7.10, a magnified view of Fig. 13(a) is given in Fig. 7.14. The shape of WGM transmission does not show any clear signs of thermally induced resonance drift and also the hot- and cold-resonance shapes are not differed by more than the linewidth of cold-resonance.

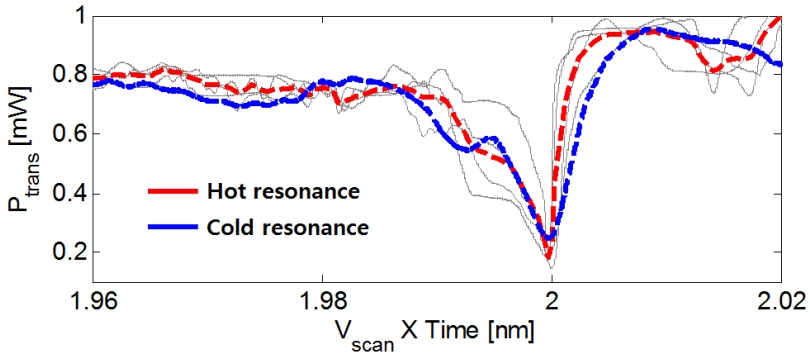

Figure 7.14. Comparison of thermally broaden WGM resonance (red) and a cold resonance (blue) measured in water medium.

To find if there is any slight temperature shift in the FBG, for $V_{scan} = 10\,pm/s$ which can potentially exhibit the largest thermal effect, each set of 5 data points in Fig. 7.13(b) is averaged and shown in Fig. 7.15 (magenta curves at bottom). The enhanced resolution shows that there is ~1.3 pm of Bragg wavelength shift (corresponds to $\Delta T \sim 0.13^{o}C$) appears when a strong WGM power presents in the resonator ($\Delta P_{in} = 1.0mW$). Red arrows in the figure are used to match the peaks of temperature shift to the corresponding WGM resonance which supplied the thermal energy.

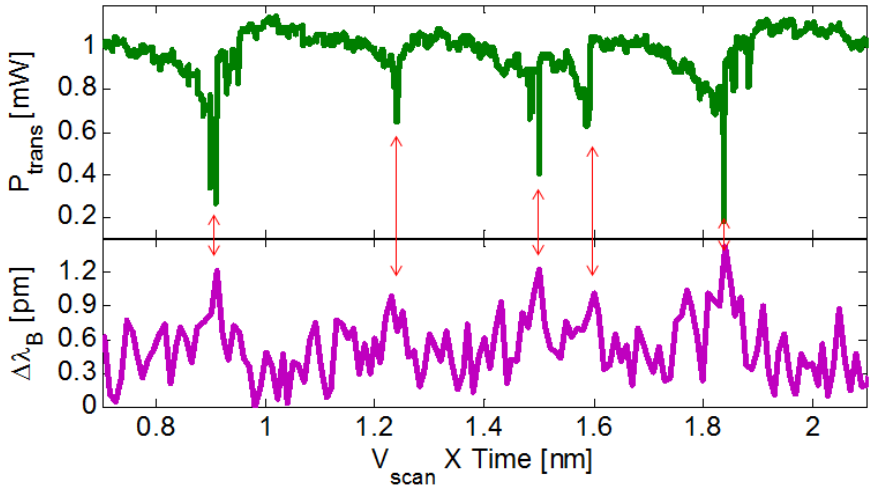

Figure 7.15. Fiber WGM transmission (top, green) and Bragg wavelength shift (bottom, magenta) measured in water medium at V_{scan} = 10 pm. Each set of 5 data points in FBG measurement are averaged.

Our study of using a FBG based optical fiber resonator has proven that the magnitude of WGM-induced thermal effect in water is suppressed by a factor of ~ 50 ($(\Delta T_{air} / \Delta P_{in,air}) / (\Delta T_{water} / \Delta P_{in,water})$) compared to the air medium case. Such a comparative analysis could not have been independently made with the conventional analysis of thermally induced WGM resonance shift. This result can also lead us to an important discussion regarding the radiation pressure induced nonlinearity discussed in chapter 6. Recently there was a study reported in [21], where the WGM characteristic of fluidic droplet in air medium is discussed. The experimental result shows that a high-*Q* WGM induces a temperature increase in the droplet resonator, and accordingly, blue-shifted resonance observed in the WGM spectrum. (Due to the negative thermo-optic coefficient of typical liquid materials, the WGM resonance in fluidic droplet resonator shifts towards shorter wavelength when there is an increase in temperature.) Though the fundamental principle of our experiment is not quite different from this study, by testing the droplet resonator in water, we observe a red-shift in WGM resonance which is induced by radiation pressure. Therefore we can deduce the critical difference between the result of [21] and ours as follows: as suggested by our FBG based WGM measurement, the test of WGM resonator in water medium can decrease the thermal nonlinearity by a significant amount. For a study of high-*Q* WGM, a careful choice of a cladding material (surrounding medium) with high thermal conductivity (e.g. water) can alleviate the thermal effects several orders of magnitude.

References

1. M. L. Gorodetsky, A. A. Savchenkov, and V. S. Ilchenko, "Ultimate Q of optical microsphere resonators," *Opt. Lett*. Vol. 21, No. 7, pp. 453–455, 1996.

2. J. Zhu, S. K. Ozdemir, Y.-F. Xiao, L. Li, L. He, D.-R. Cheng, and L. Yang, "On-chip single nanoparticle detection and sizing by mode splitting in an ultrahigh-Q microresonator," *Nat. Photonics*, Vol. 4, No. 1, pp. 46–49, 2010.

3. V. Zamora, A. Diez, M. V. Andres, and B. Gimeno, "Cylindrical optical microca vities: basic properties and sensor applications," *Phot. Nano. Fund. App l.*, Vol. 9, No. 2, pp. 149–158, 2011.

4. Y. Sun and X. Fan, "Optical ring resonators for biochemical and chemical sensin g," *Anal. Bioanal. Chem*., Vol. 399, No. 1, pp. 205–211, 2011.

5. T. Carmon, L. Yang, and K. J. Vahala, "Dynamical thermal behavior and thermal self-stability of microcavities," *Opt. Express*, Vol. 12, No. 20, pp. 4742-4750, Oc t. 2004.

6. V. S. Ilchenko, and M. L. Gorodetskii, "Thermal nonlinear effects in optical whis pering gallery microresonators," *Laser Phys*., Vol. 2, 1004, 1992.

7. C. Schmidt, A. Chipouline, T. Pertsch, A. Tünnermann, O. Egorov, F. Lederer, an d L. Deych, "Nonlinear thermal effects in optical microspheres at different wavel ength sweeping speeds," *Opt. Express*, Vol. 16, No. 9, pp. 6286-6301, Apr. 2008.

8. N. Vukovic, N. Healy, P. Horak, J. R. Sparks, P. J. A. Sazio, J. V. Badding, and A. C. Peacock, "Ultra-smooth microcylindrical resonators fabricated from the sili con optical fiber platform," *Appl. Phys. Lett*., Vol. 99, No. 3, 031117, 2011.

9. A. Boleininger, T. Lake, S. Hami, and C. Vallance, "Whispering gallery modes in standard optical fibres for fibre profiling measurements and sensing of unlabelle d chemical species," *Sensors (Basel)*, Vol. 10, No. 3, pp. 1765–1781, 2010.

10. P. Zhang, S. Jung, A. Lee, and Y. Xu, "Comparative analysis of nonlinear optoflu idics processes in microdroplets," *Phys. Rev. E*, Vol. 93, No. 6, 2016.

11. P. Zhang, S. Jung, A. Lee, and Y. Xu, "Radiation-pressure-induced nonlinearity i n microdroplets," *Phys. Rev. E*, Vol. 92, No. 6, 2015.

12. V. Zamora, A. Diez, M. V. Andres, and B. Gimeno, "Interrogation of whispering-gallery modes resonances in cylindrical microcavities by backreflection detectio n," *Opt. Letters*, Vol. 34, No. 7, pp. 1039-1041, Apr. 2009.

13. A. W. Poon, R. K. Chang, and J. A. Lock, “Spiral morphology-dependent resona nces in an optical fiber: effects of fiber tilt and focused Gaussian beam illuminati on,” *Opt. Letters*, Vol. 23, No. 14, pp. 1105-1107, July 1998.

14. I. Teraoka, “Analysis of thermal stabilization of whispering gallery mode resonan ce”, *Opt. Comm.*, Vol. 310, pp. 212-216, 2014.

15. M. H.-Zadeh and K. J. Vahala, “Fiber-taper coupling to Whispering-Gallery mod es of fluidic resonators embedded in a liquid medium,” *Opt. Express*, Vol. 14, No. 22, pp. 10800-10810, Oct. 2006.

16. R. Kitamura, L. Pilon, and M. Jonasz, “Optical constants of silica glass from extr eme ultraviolet to far infrared at near room temperature,” *Appl. Opt.*, Vol. 46, No. 33, pp. 8118-8133, Nov. 2007.

17. G. M. Hale and M. R. Querry, “Optical Constants of Water in the 200-nm to 200u m Wavelength Region,” *Appl. Opt.*, Vol. 12, No. 3, pp. 555-563, March 1973.

18. David N. Nikogosyan, “Properties of Optical and Laser Related Materials A Han dbook,” (John Wiley & Son,1997).

19. Incropera, F. and Dewitt, D., 1996, “Introduction to Heat ransfer,” New York: Wi ley.

20. Yunus A. Ç engel (2003). “Heat Transfer: a Practical Approach (2nd ed.),” McGr aw-Hill.

21. S. Maayani, L. L. Martin, and T. Carmon, “Water-walled microfluidics for high-optical finesse cavities,” *Nat. Comm.*, Vol. 10, 1038, Jan. 2016.

Chapter 8

Discussion, Future Works

8.1 Feasibility of Single-photon-level Nonlinearity

Our results confirmed that the radiation pressure of the WGM can deform the liquid droplet and significantly modify its transmission spectrum. The dynamics of the nonlinear optofluidic system is governed by Eq. (4.11), where the WGM and the droplet are coupled together via radiation pressure. For a $\sim 500 \mu m$-diameter droplet of index matching fluid immersed in water, we found that experimental data are in good agreement with the HO model's predictions, where we used two fitting parameters: $\mu = 15.3\, mPa \cdot s$ and $\sigma = 18\, mN/m$. These two values are close to material properties of the index matching fluid given by its specification sheet.

The most interesting possibility of radiation pressure induced droplet deformation is single photon nonlinearity [1]. Fig. 8.1(a) shows the saturation power P_{sat} for droplets with different radii, where we considers liquids with normal ($\sigma = 18\, mN/m$) as well as two ultralow interfacial tensions ($\sigma = 10^{-2}$ and 10^{-4} mN/m). We increase the index contrast ($\Delta n = 0.45$) to ensure that the droplet can maintain high-Q factor for R_0 as small as 10 μm. (The value of P_{sat} does not depend significantly on index contrast).

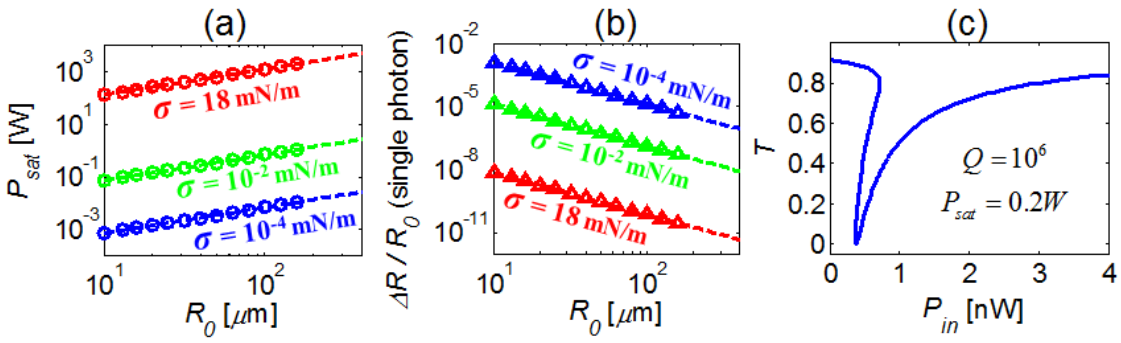

Figure 8.1. (a) The saturation power P_{sat} for droplets with different radii and surface tensions. (b) The change of droplet radius due to the presence of a single-photon versus droplet radius at different interfacial tensions. (c) Optical bistability for a 30μm droplet with low interfacial tension (10^{-2} mN/m).

Fig. 8.1(b) shows the magnitude of droplet deformation induced by the radiation pressure of a single photon, where we set the total energy within the WGM to $\hbar\omega$. Two features are immediately obvious from Fig. 8.1(a) and 8.1(b). First the strength of nonlinearity is inversely proportional to the σ. Second, the effective nonlinearity scales as $\sim 1/R_0^2$, and is much stronger for smaller droplets. For a liquid droplet with $R_0 \sim 30\mu m$ and $\sigma = 10^{-2} mN/m$, the presence of a single photon can generate $\Delta R \sim 39nm$ and $\Delta\lambda_{res} \sim 1nm$. Given our experimental data in chapter 6, such a large resonance shift can be easily measured. Furthermore, under such conditions, droplet deformation induced by a single photon becomes comparable to thermal fluctuations, since $\Delta R_{therm} = \sqrt{k_B T/20\sigma} \sim 5nm$. Finally, given the similarity between Kerr nonlinearity and radiation pressure induced nonlinearity, we can also expect many interesting nonlinear behaviors such as optical bistability at single-photon-energy level. For example, we can combine Eqs. (4.11), (4.12), and (4.15) and calculate the steady-state transmission coefficient of a droplet resonator with the following parameters: $R_0 \sim 30\mu m$, $Q = 10^6$, and

$\sigma = 10^{-2} mN/m$. Based on the result in Fig. 8.1(b), the saturation power of such a droplet is $P_{sat} = 0.2W$. According to the simulation result in Fig. 8.1(c), at $P_{in} \sim 0.5nW$, the transmission coefficient become multivalued, which is a characteristic feature of optical bistability. At this power level, the energy of the WGM in the droplet corresponds to approximately single-photon energy.

8.2 Future Works

8.2.1 Droplets with Ultralow Interfacial Tension

There are extensive researches reported in [2-4] regarding a water-in-oil micro-emulsion system. The liquid is a mixture that contains 9% water, 4% sodium dodecyl sulfate ($NaC_{12}H_{25}SO_4$), 70% toluene (C_7H_8), and 17% n-butanol-1 ($C_4H_{10}O$). At a temperature slightly higher than the critical temperature for phase transition ($T_c = 35^oC$), the mixture's phase separates into two different micellar phases. A photo of preliminarily tested mixture in bulk volume is shown in Fig. 8.2, where the liquid interface is clearly visible. According to [2], above the critical temperature, the interfacial tension of the micro-emulsion system is given by $\sigma = \sigma_0 (T/T_c - 1)^{2\nu}$, where $\sigma_0 = 0.1\, mN/m$ and $\nu = 0.63$. Assuming a high-Q droplet WGM resonator with such an extremely low interfacial tension, the analysis in chapter 8.1 suggests that we should be able to generate strong single-photon nonlinearity.

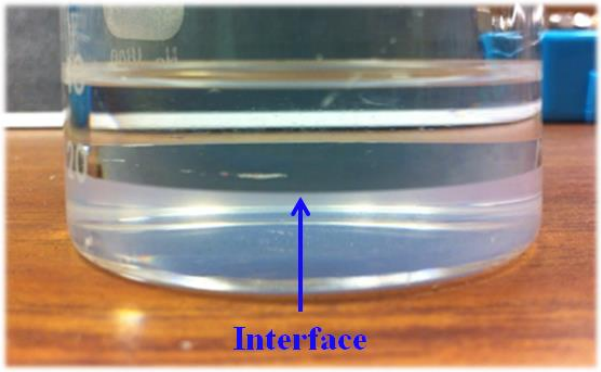

Figure 8.2. A liquid system with ultralow interfacial tension.

8.2.2 Demonstration of μW-level optical switching

An important application of nonlinear optics is optical switching, where one uses an optical beam to control the other optical beam. We can use the optical system in Fig. 8.3 to demonstrate the dynamics of radiation-pressure driven optofluidics at micro-watt level optical power.

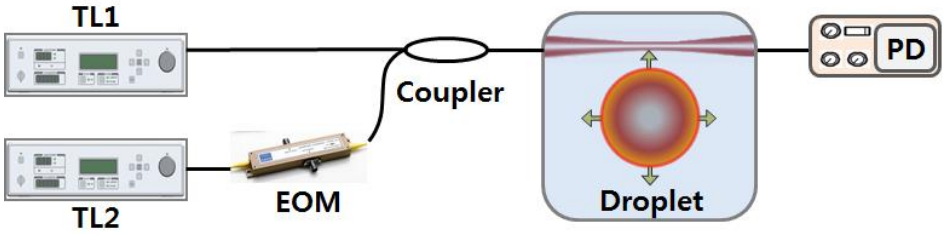

Figure 8.3. Experimental system for the demonstration of optical switching.

The operation principle of the system is as follows. We use one tunable laser (TL1) to produce a relatively high beam power to deform the droplet interface. In previous chapters, we indirectly estimated the droplet deformation by linking the shift in WGM resonance ($\Delta\lambda_{res}$) with ΔP_{in}. Here, we use another tunable laser (TL2) to measure the

WGM resonances of the deformed droplet in real time. To ensure that the laser beam generated by TL2 does not distort the droplet, we use a much lower input power for TL2. Additionally, for TL2, we will choose a high wavelength scanning speed in a narrow range. Under these conditions, we expect to measure the resonance wavelength of the deformed droplet every 0.1 to 1ms, where the speed is limited by the wavelength sweep rates of commercially available TLs. Introducing an electro-optical modulator (EOM) that shifts the phase of TL2 laser output can further improve the scanning speed. For a typical EOM with 200 ps optical rise time (PM635, Jenoptik), through appropriate phase modulation, we can effectively shift the wavelength of TL2 in a narrow spectral range ($\sim 1pm$) within a short time period (e.g., $<1\mu s$). For droplet resonators with *Q*-factor in a range of 10^6 to 10^7, the estimated $\sim 1pm$ scanning range and $<1\mu s$ scanning time is sufficient to determine the dynamics of the droplet driven by radiation pressure.

Based on our experimental results in Fig. 6.4, we expect to find that even at a relatively low input power level ($\leq 10\mu W$ for TL1 signal), the phase and amplitude of the optical signal generated by TL2 will be significantly changed by the presence of TL1 signal. In fact, using the EOM-based high speed spectral scan, we expect to find a random fluctuation of ΔR when TL1 signal is zero due to the thermal fluctuation estimated in Eq. (6.3) and other environmental noise. Yet as soon as TL1 signal excites the high-*Q* WGM in the droplet, it would be more likely to find an increase in ΔR.

References

1. Y. Xu, P. Zhang, S. Jung, and A. Lee, "Analysis of radiation pressure induced no nlinear optofluidics," *Opt. Express*, Vol. 22, pp. 28875-28889, Nov. 2014.

2. A. Casner and J.-P. Delville, "Adaptative lensing driven by the radiation pressure of a continuous-wave laser wave upon a near-critical liquid interface," *Opt. Lett.*, Vol. 26, pp. 1418-1420, 2001.

3. A. Casner, J.-P. Delville, and I. Brevik, "Asymmetric optical radiation pressure ef fects on liquid interfaces under intense illumination," *J. Opt. Soc. Am. B*, Vol. 20, pp. 2355-2362, Nov. 2003.

4. J. P. Delville, M. R. de Saint Vincent, R. D. Schroll, H. Chraibi, B. Issenmann, R. Wunenburger, et al., "Laser microfluidics: fluid actuation by light," *J. Opt. Pure Appl. Opt.*, Vol. 11, Mar. 2009.